Enhancing the Reliability of Closed-Loop Describing Function Analysis for Reset Control Applied to Precision Motion Systems

Zhang, Xinxin; HosseinNia, S. Hassan

DOI
10.1109/TCST.2025.3625632

Publication date
2026

Document Version
Final published version

Published in
IEEE Transactions on Control Systems Technology

Enhancing the Reliability of Closed-Loop Describing Function Analysis for Reset Control Applied to Precision Motion Systems

Xinxin Zhang, *Member, IEEE*, and S. Hassan HosseinNia, *Senior Member, IEEE*

***Abstract*—The sinusoidal input describing function (SIDF) is a powerful tool for control system analysis and design, with its reliability directly impacting the performance of the designed control systems. This study improves both the accuracy of SIDF analysis and the performance of closed-loop reset feedback systems through two main contributions. First, it introduces a method to identify frequency ranges where SIDF analysis becomes inaccurate. Second, these identified ranges correlate with dominated high-order harmonics that can degrade system performance. To address this, a shaped reset control strategy is proposed, incorporating a shaping filter that tunes reset actions to suppress these harmonics. A frequency-domain design procedure for the shaped reset control system is then demonstrated in a case study, where a proportional–integral–derivative (PID)-based shaping filter effectively reduces high-order harmonics and eliminates limit cycles issues under step inputs. Finally, simulations and experiments on a precision motion stage validate the shaped reset control, confirming improved SIDF analysis accuracy, enhanced steady-state performance over linear and reset controllers, and the elimination of limit cycles under step inputs.**

***Index Terms*—High-order harmonics, limit cycles, precision positioning system, reset feedback control, sinusoidal input describing function (SIDF), steady-state performance.**

I. Introduction

IN MECHATRONICS industries, such as semiconductor manufacturing, robotics, and optical systems, there is a continuous demand for enhanced positioning precision, speed, and stability [1]. Linear feedback control, particularly proportional–integral–derivative (PID) control, is widely used in these applications due to its effectiveness and ease of implementation. However, the limitations of linear controllers, including the "waterbed effect" and the Bode phase-gain trade-offs [2], undermine their transient and steady-state performance, making it challenging for them to meet the increasing performance demands in industries.

To overcome the limitations of linear controllers and address the rising industrial demands, nonlinear control strategies have been explored [3]. One such advancement is reset feedback control. Reset control originates from the Clegg integrator (CI), which is introduced by Clegg [4]. The CI is a linear integrator that incorporates a reset mechanism zero-crossing law, that resets the integrator's output to zero whenever the input signal crosses zero. The Sinusoidal-Input Describing Function (SIDF) analysis [5] reveals that the CI introduces a phase lead of 51.9°, while maintaining the gain characteristics of a linear integrator. Leveraging the gain and phase benefits, reset controllers demonstrate enhanced performance compared with linear controller, including reduced settling time, lower overshoot, and improved noise rejection in various precision motion control applications [6], [7], [8], [9], [10], [11], [12].

While reset control enhances gain-phase margins for the first-order harmonic, it also introduces high-order (beyond the first order) harmonics. To evaluate these harmonics in closed-loop reset systems, higher order sinusoidal input describing function (HOSIDF) analysis is effectively used [13], [14], [15]. The HOSIDF analysis quantifies the magnitude and phase of the harmonics in reset systems by measuring the systems' steady-state responses to sinusoidal inputs over a frequency range [13]. When only the first-order harmonic is considered and high-order harmonics are neglected, this is referred as the first-order SIDF (FOSIDF) [5]. In this study, both HOSIDF and FOSIDF are collectively termed SIDF analysis methods.

Current SIDF analysis methods for closed-loop reset systems [5], [14], [15] assume that only two reset actions per steady-state cycle in sinusoidal-input reset systems. However, sinusoidal-input closed-loop reset systems can exhibit either two reset actions or multiple (more than two) reset actions per steady-state cycle, referred to as two-reset systems and multiple-reset systems, respectively. The two-reset assumption in SIDF analysis introduces inaccuracies when applied to multiple-reset systems, as demonstrated in Section III. In such cases, the validity of the SIDF analysis is compromised, and thus the reliability of the reset control system design based on this analysis is not guaranteed.

To enhance the reliability of SIDF analysis in closed-loop reset systems, the first contribution of this study presents a method for identifying multiple-reset frequency ranges where the validity of SIDF analysis is compromised. To achieve this, we first derive piecewise expressions for the steady-state trajectories of sinusoidal-input closed-loop reset control systems. Using these expressions, a method is proposed to evaluate whether the SIDF analysis satisfies the two-reset condition in closed-loop reset systems. In previous methods,

Received 21 November 2024; revised 19 April 2025 and 3 July 2025; accepted 24 September 2025. Date of publication 12 November 2025; date of current version 30 December 2025. Recommended by Associate Editor E. Lefeber. *(Corresponding author: S. Hassan HosseinNia.)*

The authors are with the Department of Precision and Microsystems Engineering (PME), Delft University of Technology, 2628 CD Delft, The Netherlands, (e-mail: x.zhang-15@tudelft.nl; S.H.HosseinNiaKani@tudelft.nl).

This article has supplementary downloadable material available at https://doi.org/10.1109/TCST.2025.3625632, provided by the authors.

Digital Object Identifier 10.1109/TCST.2025.3625632

verifying this condition required calculating time-domain responses across the entire frequency spectrum, a process that is computationally expensive. The new method streamlines this process, offering a more efficient approach. Experimental results from two case studies confirm the effectiveness and time-saving benefits of this method.

In addition to compromising the accuracy of closed-loop SIDF analysis, multiple-reset actions in sinusoidal-input closed-loop reset systems indicate dominated high-order harmonics. These dominated high-order harmonics can increase the system's sensitivity to high-frequency noise and disturbances, leading to overall performance degradation [15].

To tackle this challenge, the second contribution of this study introduces a shaped reset control strategy that incorporates a shaping filter that enables the tuning of reset actions to reduce high-order harmonics while preserving the benefits of the first-order harmonic. A detailed design procedure for a PID-shaped reset control system is provided, aimed at reducing high-order harmonics in a CI-based reset system. In addition, the PID-shaped reset control addresses limit-cycle issues in reset systems under step inputs. Experimental results on a precision motion stage show that by decreasing the impact of high-order harmonics, the PID-shaped reset control system enhances the reliability of SIDF analysis and improves steady-state precision, including better reference tracking accuracy, disturbance rejection, and noise suppression. Moreover, it eliminates limit-cycle problems.

The remainder of this article is organized as follows. Section II provides background on reset control systems and and an overview of the experimental setup. Section III identifies two key research problems through illustrative examples, framing the study's objectives. Section IV introduces the first contribution: a method to distinguish between two-reset and multiple-reset actions in sinusoidal-input closed-loop reset systems, establishing two-reset conditions for SIDF analysis with validation through simulations and experiments. Section V presents the second contribution, proposing a shaped reset control strategy aimed at reducing high-order harmonics. Section VI outlines a design procedure for a PID shaping filter, showcased as a case study to decrease high-order harmonics and eliminate limit cycles. Section VII then provides simulation and experimental results to validate the PID-shaped reset control system's effectiveness on a precision motion stage. Finally, Section VIII summarizes the main findings and offers recommendations for future research directions.

II. Preliminaries

This section introduces the definition of the reset feedback control system, its stability and convergence conditions, the SIDF analysis method, and the experimental setup.

A. Reset Control System

This study focuses on the frequency-domain analysis and design of closed-loop reset feedback control systems, as shown in Fig. 1. The system comprises a nonlinear time-invariant reset controller $\mathcal{C}_r$ in conjunction with linear time-invariant (LTI) systems $\mathcal{C}_s$, $\mathcal{C}_1$, $\mathcal{C}_2$, $\mathcal{C}_3$, $\mathcal{C}_4$, and an LTI plant $\mathcal{P}$. The

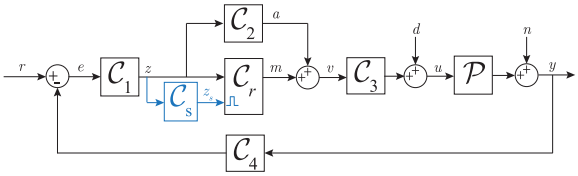

Fig. 1. Block diagram of the closed-loop reset feedback control system.

signals $r(t)$, $e(t)$, $u(t)$, $y(t)$, $a(t)$, and $v(t)$ denote the reference input, error, control input, system output, output of $\mathcal{C}_2$, and input to $\mathcal{C}_3$, respectively. The LTI system $\mathcal{C}_s$, referred to as the shaping filter in this study, is defined by state-space matrices A_s, B_s, C_s, and D_s, with $x_s(t) \in \mathbb{R}^{n_s \times 1}$, $n_s \in \mathbb{Z}^+$, denoting its state vector.

The reset controller $\mathcal{C}_r$ is a hybrid system. Its state-space representation, with $z(t)$ as the input signal, $m(t)$ as the output signal, and $x_c(t) \in \mathbb{R}^{n_c \times 1} (n_c \in \mathbb{Z}^+)$ as the state vector, is expressed as follows [16]:

$$\mathcal{C}_r = \begin{cases} \dot{x}_c(t) = A_R x_c(t) + B_R z(t), & (x_s(t), z(t)) \notin J_c \\ x_c(t^+) = A_\rho x_c(t), & (x_s(t), z(t)) \in J_c \\ m(t) = C_R x_c(t) + D_R z(t) \end{cases} \quad (1)$$

where $A_R \in \mathbb{R}^{n_c \times n_c}$, $B_R \in \mathbb{R}^{n_c \times 1}$, $C_R \in \mathbb{R}^{1 \times n_c}$, and $D_R \in \mathbb{R}^{1 \times 1}$ define the flow dynamics of the reset controller $\mathcal{C}_r$, and $A_\rho \in \mathbb{R}^{n_c \times n_c}$ characterizes its jump dynamics, given by

$$A_\rho = \begin{bmatrix} \gamma & \\ & I_{n_c-1} \end{bmatrix}, \quad \gamma \in (-1, 1) \in \mathbb{R}. \quad (2)$$

The reset set is defined as $(x_s(t), z(t)) \in J_c$, where $J_c = \{(x_s(t), z(t)) \mid x_s(t) \in \mathbb{R}^{n_s \times 1}, z(t) \in \mathbb{R}, C_s x_s(t) + D_s z(t) = 0\}$, indicating that reset actions occur when the "reset-trigger signal" $z_s(t)$ crosses zero, following the "zero-crossing law" [16].

The flow dynamics of $\mathcal{C}_r$ are characterized by the base-linear controller (BLC), described in the frequency domain as

$$C_l(\omega) = C_R (j\omega I - A_R)^{-1} B_R + D_R, \; j = \sqrt{-1}, \omega \in \mathbb{R}^+. \quad (3)$$

By substituting the reset controller $\mathcal{C}_r$ with its base-linear counterpart $\mathcal{C}_l$ as defined in (3), the system depicted in Fig. 1 is referred to as its base linear system (BLS).

B. Stability and Convergence Conditions for Reset Control Systems

Although stability and convergence are not the primary focus of this study, they are essential for the analysis and application of reset systems. These topics have been extensively explored in the literature [16], and we outline the necessary assumptions to ensure stability and convergence.

The reset controller (1) with an input signal $e(t) = |E| \sin(\omega t + \angle E)$ has a globally asymptotically stable $2\pi/\omega$-periodic solution if the following condition is satisfied [5]:

$$\left| \lambda \left(A_\rho e^{A_R \delta} \right) \right| < 1 \quad \forall \delta \in \mathbb{R}^+. \quad (4)$$

Therefore, to guarantee that there exists a steady-state solution for the SIDF analysis of the open-loop reset control system, the following assumption is introduced.

Assumption 1: The reset system (1) with input $e(t) = |E|\sin(\omega t + \angle E)$ meets the condition in (4). In addition, LTI systems $\mathcal{C}_1$, $\mathcal{C}_2$, $\mathcal{C}_3$, and $\mathcal{C}_4$ are Hurwitz.

To ensure that the frequency response of a closed-loop reset control system is well-defined, Assumption 2 is introduced to guarantee the system's stability and convergence.

Assumption 2: The closed-loop reset control system is asymptotically stable in the absence of inputs and exponentially convergent. The reset controller $\mathcal{C}_r$ in (1) has zero initial conditions, i.e., $x_c(0) = 0$. The input signals are Bohl functions as defined in [17]. Furthermore, there exist infinitely many reset instants t_i such that $\lim_{i\to\infty} t_i = \infty$, and the system does not exhibit Zeno behavior.

The stability and convergence conditions for reset control systems have been extensively studied, including the H_β condition [18], [19] and additional criteria in [20] and [21]. As these are beyond the scope of this article, they are not discussed in detail. Nevertheless, Assumption 2 can be achieved through careful system design, as demonstrated in [14] and [16].

C. Sidf Analysis for Open-Loop Reset Control Systems

For an open-loop reset system in Fig. 1 with the input $e(t) = |E|\sin(\omega t + \angle E)$ and the output $y(t)$, satisfying Assumption 1, let $E(\omega)$ and $Y_1(\omega)$ represent the Fourier transforms of the input signal $e(t)$ and the first-order harmonic component of the output signal $y(t)$, respectively. Define

$$\begin{aligned}
\Delta(\omega) &= I + e^{\left(\frac{\pi}{\omega}A_R\right)} \\
\Delta_r(\omega) &= I + A_\rho e^{\left(\frac{\pi}{\omega}A_R\right)} \\
\Omega(\omega) &= \Delta(\omega) - \Delta(\omega)\,{\Delta_r}^{-1}(\omega)\,A_\rho\Delta(\omega) \\
\mathcal{C}_r^1(\omega) &= C_R\left(A_R - j\omega I\right)^{-1}\Theta_\phi(\omega) + \mathcal{C}_{\text{bl}}(\omega) \\
\Theta_\phi(\omega) &= -2j\omega I e^{j\angle\mathcal{C}_s(\omega)}\Omega(\omega)/\pi \cdot [\omega I\cos(\angle\mathcal{C}_s(\omega)) \\
&\quad - A_R\sin(\angle\mathcal{C}_s(\omega))]\left(\omega^2 I + {A_R}^2\right)^{-1} B_R. \qquad (5)
\end{aligned}$$

Using the SIDF analysis method [22], the first-order transfer function of the open-loop reset system, $L_1(\omega)$, is expressed as

$$L_1(\omega) = \frac{Y_1(\omega)}{E(\omega)} = \mathcal{C}_1(\omega)\left(\mathcal{C}_r^1(\omega) + \mathcal{C}_2(\omega)\right)\mathcal{C}_3(\omega)\mathcal{P}(\omega). \quad (6)$$

In this study, the crossover frequency ω_{BW} of $L_1(\omega)$ where $|L_1(\omega_{\text{BW}})| = 0$ dB in (6), is defined as the bandwidth frequency of a reset control system.

D. Precision Motion Stage

This article addresses the challenge of performance in reset feedback control systems related to SIDF analysis, which is crucial for precision motion control applications. When the reliability of the SIDF frequency response analysis for closed-loop reset systems is compromised, it results in uncertainty regarding the precision of the designed reset control system. In addition, the frequency ranges where SIDF analysis is compromised correspond to regions with high-order harmonics. If these harmonics are not properly managed in reset systems, they can cause oscillations due to high-frequency noise. Such oscillations can degrade system precision, negatively affecting stability and overall performance.

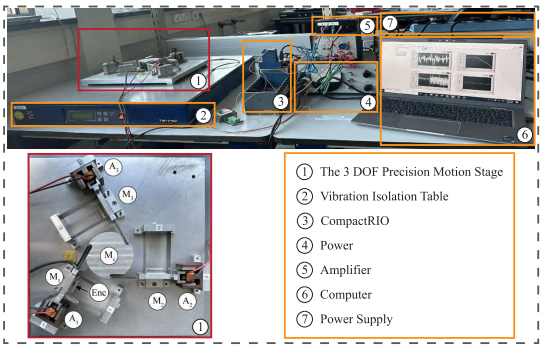

Fig. 2. Experimental precision positioning setup.

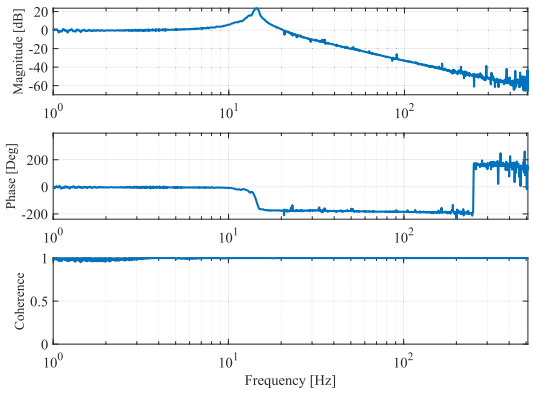

Fig. 3. FRF data from actuator A_1 to attached mass M_1.

The precision motion setup used in this study is shown in Fig. 2. The motion stage is a 3 degree-of-freedom (DoF) system with three masses (M_1, M_2, and M_3), actuated by three voice coil actuators (A_1, A_2, and A_3). These masses are connected to a central base (M_c) via dual leaf flexures, which provide the necessary flexibility for precise motion. The actuators are driven by a linear current–source power amplifier. The control systems for this stage are implemented on an NI compactRIO platform, which includes field-programmable gate array (FPGA) modules for real-time processing. The digital control utilizes the Tustin discretization method. Position feedback is provided by a Mercury M2000 linear encoder (labeled as Enc, offering a high-resolution measurement of 100 nm, with the data sampled at a rate of 10 kHz.

In this study, the pair of actuator A_1 and mass M_1 are utilized. Fig. 3 shows the measured frequency response function (FRF) from actuator A_1 to mass M_1. The FRF data characterize a collocated double mass-spring-damper system with high-frequency parasitic dynamics.

Using the system identification tools in MATLAB, the system is modeled as an LTI system represented by

$$\mathcal{P}(s) = \frac{6.615 \times 10^5}{83.57s^2 + 279.4s + 5.837 \times 10^5}. \qquad (7)$$

This model represents the core behavior of the actuator-mass system and is used for the design and analysis of the reset control strategies discussed in the article.

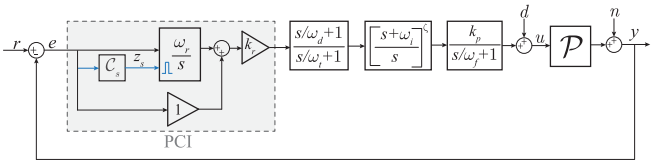

Fig. 4. Block diagram of the reset PID control system.

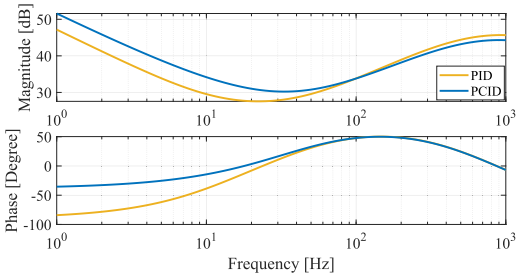

Fig. 5. Bode plots of the PID and the first-order harmonic of the PCID control systems.

III. Motivation and Problems Statement via Illustrative Examples

This section outlines two research problems through examples. The first problem is that the precision of SIDF analysis is compromised by multiple-reset actions. The second problem is that these actions relate to high-order harmonics in the system, which, if large, can degrade overall system performance.

To illustrate these two problems, we design a reset control system as an example. The generalized CI is defined by (1) with the matrices $A_\rho = \gamma \in (-1, 1)$ and $(A_R, B_R, C_R, D_R) = (0, 1, 1, 0)$. A CI-based reset controller is a reset element designed using built on this generalized CI. PID controllers are widely used in mechatronics applications, and when the integrator in the PID controller is replaced by the generalized CI, the system becomes a reset PID control system. This section uses a reset PID control system to demonstrate the research problems addressed in this study.

The block diagram of the reset PID control system used in this study is depicted in Fig. 4. The parameter ζ denotes the number of integrators in the system, with this study utilizes cases where $\zeta = 0$ and $\zeta = 1$, referred to as proportional-CI-derivative (PCID) and PCI-PID control systems, respectively. More discussion on employing multiple integrators ($\zeta > 1$) is beyond the scope of this article and can be found in [23].

A PCID control system is designed as the illustrative example with the following parameters: $k_p = 17.8$, $\omega_c = 300\pi$ [rad/s], $\omega_r = 0.1\omega_c$, $k_r = 0.85$, $\gamma = 0$, $\omega_d = \omega_c/3.8$, $\omega_t = 3.8\omega_c$, $\omega_f = 10\omega_c$, $\zeta = 0$, and $\mathcal{C}_s = 1$. A PID controller is also designed for comparison with the following parameters: $k_p = 17.8$, $\omega_c = 300\pi$ [rad/s], $\omega_i = 0.084\omega_c$, $\omega_d = \omega_c/3.8$, $\omega_t = 3.8\omega_c$, and $\omega_f = 10\omega_c$.

The Bode plots for the PID and the first-order harmonic of the PCID control systems are presented in Fig. 5. To ensure a fair comparison, both the PID and PCID controllers are designed to maintain the same bandwidth of 100 Hz and a phase margin of 50° with the plant $\mathcal{P}(s)$ in (7). However, the PCID controller exhibits a higher gain at frequencies below 100 Hz and a reduced gain at frequencies above 100 Hz. This design aims to enhance low-frequency tracking and disturbance rejection, and high-frequency noise suppression.

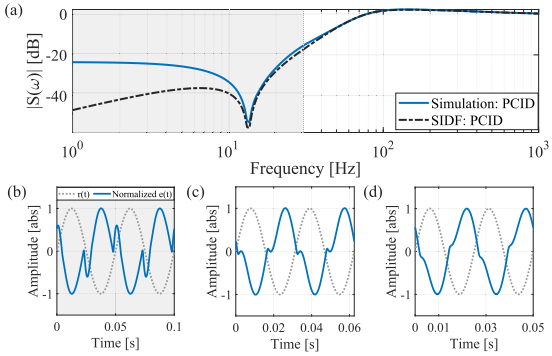

Fig. 6. (a) Magnitude $|\mathcal{S}(\omega)|$ for the PCID control system, derived from simulation and SIDF analysis. The multiple-reset and two-reset systems are represented by gray and white shading, respectively. Normalized steady-state errors of the system under sinusoidal inputs $r(t) = \sin(2\pi ft)$ with (b) $f = 20$ Hz, (c) $f = 32$ Hz, and (d) $f = 40$ Hz.

A. Problem 1: Multiple-Reset Actions Leading to Inaccuracies in Closed-Loop Sidf Analysis

To evaluate the performance of closed-loop reset control systems, SIDF analysis is often employed. For closed-loop reset systems with a sinusoidal input $r(t) = |R|\sin(\omega t)$, which satisfies Assumption 2, the sensitivity function based on SIDF analysis [5], [22], is defined as follows:

$$\mathcal{S}(\omega) = 1/(1 + L_1(\omega)) \tag{8}$$

where $L_1(\omega)$ is defined in (6).

The magnitude of the closed-loop sensitivity function $|\mathcal{S}(\omega)|$ for the PCID control system, analyzed using (8), is presented in Fig. 6(a). This analytical result is compared with the simulated value of $|\mathcal{S}(\omega)|$, which is calculated as $\|e\|_\infty/\|r\|_\infty$ at each frequency ω, where $e(t)$ represents the steady-state error and $r(t)$ denotes the input signal.

In closed-loop reset systems with a sinusoidal reference input $r(t) = |R|\sin(\omega t)$, a two-reset system is defined by exactly two reset events within each $2\pi/\omega$ steady-state cycle, whereas a multiple-reset system has more than two reset events per cycle. For instance, Fig. 6(b)–(d) shows the simulated steady-state errors under sinusoidal inputs $r(t) = \sin(2\pi ft)$ at $f = 20$ Hz, $f = 32$ Hz, and $f = 40$ Hz, corresponding to a multiple-reset system, the transition region between multiple- and two-reset systems, and a two-reset system, respectively. In Fig. 6(a), the region associated with multiple-reset systems is shaded in gray, where notable discrepancies between SIDF analysis and simulation results are observed. These differences arise because the two-reset assumption in the SIDF analysis, does not hold in systems exhibiting multiple-reset actions.

Hence, to ensure the reliability of the SIDF analysis for closed-loop reset systems, it is crucial to establish a two-reset condition. The first contribution of this study in Section IV addresses this issue. Consider a closed-loop reset system subjected to a sinusoidal input signal defined by $r(t) = |R|\sin(\omega t)$,

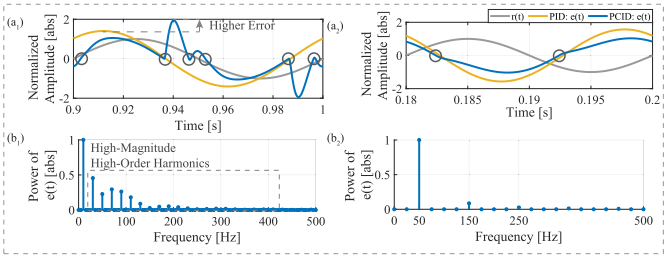

Fig. 7. Steady-state errors $e(t)$ for the PID and PCID systems under two input signals: (a_1) $r(t) = \sin(20\pi t)$ and (a_2) $r(t) = \sin(100\pi t)$. The gray circles mark the reset instants per cycle. Panels (b_1) and (b_2) display the PSD plots for the errors $e(t)$ in (a_1) and (a_2), respectively.

where $|R|$ represents the amplitude and ω denotes the frequency. As ω sweeps through the operational frequency range, the proposed method identifies the frequency ranges where multiple-reset actions occur and thus deviations occur in the SIDF analysis, as illustrated by the gray area in Fig. 6(a).

B. Problem 2: Multiple-Reset Actions Relating to High-Order Harmonics That Need to Be Reduced

In addition to introducing imprecision in SIDF analysis, multiple-reset actions in a sinusoidal-input closed-loop reset system indicate high-magnitude high-order (beyond first-order) harmonics [14], [15]. These large high-order harmonics can adversely affect overall system performance. This detrimental effect is further illustrated in Fig. 7.

The steady-state errors of the closed-loop PCID and PID control systems, subjected to sinusoidal reference inputs $r(t) = \sin(20\pi t)$ (10 Hz) and $r(t) = \sin(100\pi t)$ (50 Hz), are illustrated in Fig. 7. In addition, the corresponding power spectral density (PSD) plots are presented. To facilitate a clearer comparison, the magnitude of the first-order harmonic of the steady-state error in the PCID control system is normalized to 1, with the same scaling factor applied to the PID control system for fair comparison.

At an input frequency of 50 Hz, as shown in Fig. 7(b_2), the first-order harmonic component dominates, and the magnitudes of the high-order harmonics are relatively small. In this scenario, as illustrated in Fig. 7(a_2), the PCID control system demonstrates two-reset actions and a lower steady-state error compared with the PID control system.

In contrast, at an input frequency of 10 Hz, the error signal exhibits multiple reset instants as shown in Fig. 7(a_1), which are associated with the presence of high-magnitude, high-order harmonics in Fig. 7(b_1). These high-magnitude high-order harmonics diminish the benefits of the first-order harmonic in the PCID control system, leading to a larger steady-state error compared with the linear PID control system in Fig. 7(a_1).

Thus, this work introduces a shaped reset control strategy to address the adverse effects of dominated high-order harmonics, as detailed in Section V.

Note that though the practical applications extend beyond sinusoidal-input systems, the sinusoidal-input analysis serves as an effective tool for investigating the frequency-domain harmonic characteristics within these reset control systems.

IV. Identifying Two-Reset Conditions in SIDF Analysis and Experimental Validation

In this section, first, Lemma 1 presents the piecewise expressions of steady-state trajectories in sinusoidal-input closed-loop reset systems. Then, building on these expressions, Theorem 1 introduces a method to identify frequency ranges of multiple-reset and two-reset actions in sinusoidal-input closed-loop reset systems. Finally, simulations and experiments validate the effectiveness of the approach in Theorem 1.

A. Piecewise Expressions for Steady-State Trajectories in Sinusoidal-Input Closed-Loop Reset Control Systems

Consider a closed-loop reset system with a sinusoidal input $r(t) = |R|\sin(\omega t)$ that satisfies Assumption 2. In order to conduct steady-state analysis, it is crucial to establish a reference point for one steady-state cycle. This reference point $t_0 = 0$ is defined at the time instant where $r(t_0) = 0$ and $\dot{r}(t_0) > 0$. Define

$$\begin{aligned}
\mathcal{L}_{\mathrm{bl}}(\omega) &= \mathcal{C}_1(\omega)\left(\mathcal{C}_l(\omega) + \mathcal{C}_2(\omega)\right)\mathcal{C}_3(\omega)\mathcal{P}(\omega)\mathcal{C}_4(\omega)\\
\mathcal{S}_{\mathrm{bl}}(\omega) &= 1/\left(1 + \mathcal{L}_{\mathrm{bl}}(\omega)\right)\\
\mathcal{T}_s(\omega) &= \mathcal{S}_{\mathrm{bl}}(\omega)\left(j\omega I - A_R\right)^{-1}\left(A_\rho - I\right)\\
\mathcal{C}_\sigma(\omega) &= \mathcal{C}_3(\omega)\mathcal{P}(\omega)\mathcal{C}_4(\omega)\mathcal{C}_1(\omega)\\
\mathcal{T}_\alpha(\omega) &= \mathcal{C}_\sigma(\omega)C_R\mathcal{T}_s(\omega)\\
h_s(t) &= \mathscr{F}^{-1}\left[\mathcal{T}_s(\omega)\right]\\
h_\alpha(t) &= \mathscr{F}^{-1}\left[\mathcal{T}_\alpha(\omega)\right], \quad h_\beta(t) = \mathscr{F}^{-1}\left[\mathcal{C}_s(\omega)\mathcal{T}_\alpha(\omega)\right].
\end{aligned} \tag{9}$$

Lemma 1 provides a piecewise expression of steady-state trajectories in sinusoidal-input closed-loop reset systems.

Lemma 1: Consider a closed-loop reset control system as shown in Fig. 1, with a sinusoidal reference input $r(t) = |R|\sin(\omega t)$, and satisfying Assumptions 2. Within one steady-state period $(0, 2\pi/\omega]$, the reset instant t_i, at which $z_s(t_i) = 0$, divides the system trajectories into piecewise functions. Let $x_i(t)$, $z_i(t)$, and $z_s^i(t)$ denote the state, reset input, and reset-triggered signal, within the intervals $(t_{i-1}, t_i]$, where $i \in \mathbb{Z}^+$, respectively. They are expressed as follows:

$$\begin{aligned}
x_{i+1}(t) &= x_i(t) - h_s(t - t_i)\,x_i(t_i)\\
z_{i+1}(t) &= z_i(t) - h_\alpha(t - t_i)\,x_i(t_i)\\
z_s^{i+1}(t) &= z_s^i(t) - h_\beta(t - t_1)\,x_i(t_i)
\end{aligned} \tag{10}$$

Proof: The proof is provided in Appendix A. □

B. Identifying Multiple-Reset and Two-Reset Actions in Sinusoidal-Input Closed-Loop Reset Control Systems

Consider a closed-loop reset system with a sinusoidal input $r(t) = |R|\sin(\omega t)$ that satisfies Assumption 2. Let t_1 denote the first reset instant within a single steady-state cycle. Prior to reaching steady state, the system exhibits transient responses. Within the steady-state interval $(0, t_1)$, the trajectories of the reset controller are determined by both the dynamics of its BLS, as described in (3), and transient effects. To simplify the steady-state analysis and mitigate the complexity associated with modeling transient behavior, Assumption 3 asserts that

the transient effects within the interval $(0, t_1)$ are negligible, and that the reset system behaves equivalently to its BLS over this interval.

Assumption 3: The closed-loop reset control system depicted in Fig. 1, under the sinusoidal reference input $r(t) = |R|\sin(\omega t)$ and satisfying Assumption 2, follows the same steady-state trajectory as its BLS during the time interval $(0, t_1)$, where t_1 represents the first reset instant of this system within one steady-state cycle.

Assumption 3 may introduce deviations in multiple-reset system identification due to transient effects. In practical reset system designs, these transient effects are often mitigated using strategies such as feedforward control and high-bandwidth feedback loops. Moreover, the case studies in Section IV-C assess these deviations.

Define

$$\begin{aligned}
\text{sign}(x) &= \begin{cases} 0, & \text{if } x > 0 \\ 1, & \text{if } x \le 0 \end{cases} \\
\mathcal{S}_{\text{ls}}(\omega) &= \mathcal{C}_s(\omega)\mathcal{C}_1(\omega)\mathcal{S}_{\text{bl}}(\omega) \\
\Theta_{\text{bl}}(\omega) &= (j\omega I - A_R)^{-1} B_R \mathcal{C}_1(\omega)\mathcal{S}_{\text{bl}}(\omega) \\
t_m &= \angle\mathcal{S}_{\text{ls}}(\omega)/\omega + \pi/\omega \cdot \text{sign}(\mathcal{S}_{\text{ls}}(\omega)) \\
\Theta_s(\omega) &= |\Theta_{\text{bl}}(\omega)| \sin(\angle\mathcal{S}_{\text{ls}}(\omega) - \angle\Theta_{\text{bl}}(\omega)).
\end{aligned} \tag{11}$$

Then, Theorem 1 and Remark 1 delineate the condition for ensuring the two-reset assumption in the SIDF analysis methods (see [5], [14], [15]) for closed-loop reset control systems.

Theorem 1: Consider a closed-loop reset control system illustrated in Fig. 1 with a sinusoidal reference input $r(t) = |R|\sin(\omega t)$, satisfying Assumptions 2 and 3. The system is a multiple-reset system if there exists at least one time instant $t_\delta \in (0, t_m)$, such that

$$\Delta(t_\delta) = |\mathcal{S}_{\text{ls}}(\omega)| \sin(\omega t_\delta) + h_\beta(t_\delta)\Theta_s(\omega) = 0 \tag{12}$$

where $\mathcal{S}_{\text{ls}}(\omega)$ and $\Theta_s(\omega)$ are given in (11), and $h_\beta(t)$ is given in (9).

Proof: The proof is provided in Appendix B. □

Theorem 1 is applicable to model-based reset control. To use it, first, the FRF data of the plant $\mathcal{P}(s)$, is measured, and system identification methods are employed to derive the system model. Then, Theorem 1 is applied to identify the multiple-reset frequency range in sinusoidal-input closed-loop reset systems. However, if the system identification is inaccurate, the accuracy of Theorem 1 may also be compromised. In addition, deviations may arise from Assumption 3 if the transient response exhibits a large impact on the steady-state behavior. These deviations will be discussed and validated through case studies in Section IV-C.

Based on Theorem 1, Remark 1 establishes the two-reset condition for the SIDF analysis of closed-loop reset systems.

Remark 1: The SIDF analysis for closed-loop reset systems assumes a two-reset condition. This condition holds if, for all frequencies ω within the SIDF analysis frequency range, the criteria outlined in Theorem 1 are not met.

TABLE I

THEOREM 1-PREDICTED AND SIMULATED BOUNDARY FREQUENCIES f_b AND f_b' THAT SEPARATE THE TWO-RESET AND MULTIPLE-RESET SYSTEMS, AS WELL AS THE COMPUTATION TIME IN CASE_1 TO CASE_2

Systems	f_b [Hz]	f_b' [Hz]	$\lvert f_b - f_b' \rvert$ [Hz]	Prediction Time [s]	Simulation Time [s]
Case_1	30	32	2	1.38	356.63
Case_2	38	42	4	0.96	370.60

C. Simulations and Experimental Validation of Theorem 1

To validate Theorem 1, two CI-based reset controllers are designed and implemented on the precision motion system $\mathcal{P}(s)$ defined in (7) as case studies. CI-based reset control systems are chosen for this validation because they are easily implemented within the classical PID control framework, but they often encounter multiple-reset actions in SIDF analysis [14]. Ensuring the reliability of their SIDF analysis would facilitate their practical application. The systems are configured with the following parameters.

1) *Case_1:* A PCID control system, using the same design parameters outlined in Section III.
2) *Case_2:* $\mathcal{C}_r$ is built on a BLC $\mathcal{C}_l = (30\pi)/s$ with the reset value $\gamma = 0$, $\mathcal{C}_1(s) = 1/(s/(150\pi) + 1)$, $\mathcal{C}_s(s) = (s+1)/(s+2)$, $\mathcal{C}_2(s) = 1$, $\mathcal{C}_3(s) = 20.5 \cdot (s/(150\pi) + 1)/(s/(3000\pi) + 1) \cdot (s/(62.5\pi) + 1)/(s/(1440\pi) + 1) \cdot (1 + 15\pi/s) \cdot 1/(s/(3000\pi) + 1)$.

The stability and convergence of these two cases are verified using the conditions presented in [21], as provided in the supplementary material.

In these two case studies, multiple-reset actions occur at frequencies below a certain frequency, denoted f_b in predictions from Theorem 1 and as f_b' in simulations, with deviations $|f_b - f_b'|$ summarized in Table I. Both prediction and simulation methods sweep the frequency range from 1 Hz to 50 Hz with a step of 1 Hz. At each frequency, the sampling rate is set to 10^4. The results show discrepancies between 1 and 4 Hz across the cases, primarily due to the exclusion of transient response effects, as outlined in Assumption 3. In practice, these transient effects can be mitigated using strategies such as ensuring an appropriate bandwidth in the feedback loop and implementing feedforward techniques. Moreover, despite deviations of 1–4 Hz between the simulation results and the predictions from Theorem 1, the prediction method offers substantial time-saving benefits. Identifying multiple-reset occurrences through simulation or using the numerical method in [20] requires calculating the time response at each frequency across the entire operational frequency range via a `for` loop in MATLAB, followed by counting the reset instants per steady-state cycle. In contrast, Theorem 1 streamlines this process. Table I presents a comparison of computation times for the prediction and simulation methods. Results show that Theorem 1 achieves a reduction in computation time by around 300-fold compared with the simulation approach.

If extremely precise identification of multiple-reset actions is needed, Theorem 1 can be utilized for initial estimation. Subsequent simulations can then focus on the predicted frequency range, ensuring both accuracy and efficiency in pinpointing multiple-reset occurrences.

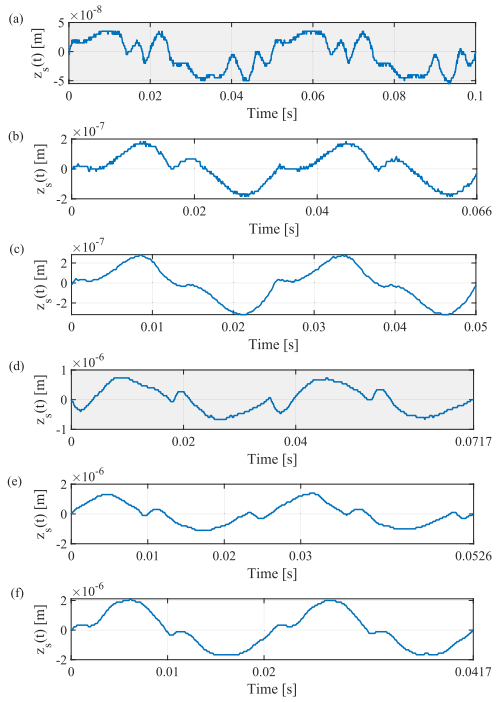

Fig. 8. Experimentally measured steady-state reset-triggered signal $z_s(t)$ for Case$_1$ with input frequencies of (a) 20 Hz, (b) f_b = 30 Hz, and (c) 40 Hz. Steady-state reset-triggered signal $z_s(t)$ for Case$_2$ with input frequencies of (d) 28 Hz, (e) f_b = 38 Hz, and (f) 48 Hz. Gray-shaded regions indicate multiple-reset systems.

To further validate Theorem 1, Fig. 8 presents experimentally measured reset-triggered signals $z_s(t)$ for systems Case$_1$ and Case$_6$ in response to a reference input of $r(t) = 1\times10^{-6}\sin(2\pi ft)$ [m]. Testing was conducted at the predicted threshold frequency $f = f_b$ Hz, as well as at $f = f_b \pm 10$ Hz, over two steady-state cycles. The results show that at (f_b-10) Hz, the systems exhibit multiple-reset behavior, while at $(f_b + 10)$ Hz, they display two reset instants per cycle, characteristic of a two-reset system. At the predicted threshold frequency f_b, the systems demonstrate 3–4 reset instants per cycle, indicating a transitional behavior between two-reset and multiple-reset categories. These observations confirm that f_b serves as a boundary frequency for distinguishing two-reset from multiple-reset actions, thereby validating Theorem 1 within a 10-Hz tolerance.

V. Analysis and Design of Shaped Reset Systems

Multiple-reset actions in sinusoidal-input closed-loop reset systems are indicative of dominated high-order harmonics. To reduce these harmonics, this section introduces a shaped reset control strategy. First, Lemma 2 provides an analytical decomposition of the steady-state reset-triggered signal $z_s(t)$ in such systems into a base-linear trajectory and a nonlinear component. Building on this, Theorem 2 defines a function $\beta_n(\omega)$, which quantifies the presence of high-order harmonics in $z_s(t)$. This function serves as the foundation for designing a shaped reset control approach to reduce high-order harmonics.

Lemma 2: Consider a closed-loop reset control system as shown in Fig. 1, with a sinusoidal reference input $r(t) = |R|\sin(\omega t)$ and adhering to Assumptions 2 and 3. Let μ denote the number of reset instants occurring within a half π/ω-cycle. Define

$$\mathcal{T}_\beta(n\omega) = \mathcal{T}_\alpha(n\omega)\cdot jn\omega$$
$$D_s^n(\omega) = \frac{2\left(A_\rho - I\right)}{n\pi}\sum_{i=1}^{i=\mu}\mathscr{F}\left[x(t_i)\sin\left(n\omega(t-t_i)\right)\right]. \quad (13)$$

In this system, the steady-state reset-triggered signal $z_s(t)$ is composed of two components: a base-linear element $z_{\mathrm{bl}}(t)$ and a nonlinear element $z_{\mathrm{nl}}(t)$, expressed as

$$z_s(t) = z_{\mathrm{bl}}(t) + z_{\mathrm{nl}}(t)$$
$$z_{\mathrm{bl}}(t) = |R|\cdot|\mathcal{S}_{\mathrm{ls}}(\omega)|\sin\left(\omega t + \angle\mathcal{S}_{\mathrm{ls}}(\omega)\right)$$
$$z_{\mathrm{nl}}(t) = -\sum_{n=1}^{\infty}\mathscr{F}^{-1}\left[\mathcal{C}_s(n\omega)\mathcal{T}_\beta(n\omega)D_s^n(\omega)\right]. \quad (14)$$

In (14) and (13), $\mathcal{T}_\alpha(\omega)$ and $\mathcal{S}_{\mathrm{ls}}(\omega)$ are defined as in (9) and (11), respectively, and $x(t_i)$ denotes the state of the reset controller $\mathcal{C}_r$ at the reset instant t_i.

Proof: The proof is provided in Appendix C. □

In the reset-triggered signal $z_s(t)$, the nonlinear component $z_{\mathrm{nl}}(t)$ in (14) can be represented as the sum of its harmonic components, expressed as

$$z_{\mathrm{nl}}(t) = \sum_{n=1}^{\infty} z_{\mathrm{nl}}^n(t)$$
$$z_{\mathrm{nl}}^n(t) = \sum_{n=1}^{\infty}\left|Z_{\mathrm{nl}}^n\right|\sin\left(n\omega t + \angle Z_{\mathrm{nl}}^n\right) \quad (15)$$

where $|Z_{\mathrm{nl}}^n|$ and $\angle Z_{\mathrm{nl}}^n$ represent the magnitude and the phase of the signal $z_{\mathrm{nl}}^n(t)$.

Let $Z_{\mathrm{nl}}^n(\omega)$ represent the Fourier transform of the n-th harmonic $z_{\mathrm{nl}}^n(t)$ within $z_{\mathrm{nl}}(t)$. The following theorem provides the magnitude ratio of the higher order harmonics ($n > 1$) to the first-order harmonic ($n = 1$) in $z_{\mathrm{nl}}(t)$.

Theorem 2: Consider the closed-loop reset control system depicted in Fig. 1, with a sinusoidal reference input $r(t) = |R|\sin(\omega t)$, and assume it satisfies Assumptions 2 and 3. At the input frequency ω, the magnitude ratio of the higher order harmonics (where $n > 1$) to the first-order harmonic (where $n = 1$) in $z_{\mathrm{nl}}(t)$ in (14) is given by

$$\beta_n(\omega) = \frac{\left|Z_{\mathrm{nl}}^n(\omega)\right|}{\left|Z_{\mathrm{nl}}^1(\omega)\right|} = \frac{\left|\mathcal{C}_s(n\omega)\mathcal{T}_\beta(n\omega)\right|}{n\left|\mathcal{C}_s(\omega)\mathcal{T}_\beta(\omega)\right|}, \quad \text{where } n > 1. \quad (16)$$

Proof: The proof is provided in Appendix D. □

Remark 2: According to Theorem 2, when $\beta_n(\omega) \to 0$, $|Z_{\mathrm{nl}}^n(\omega)| \ll |Z_{\mathrm{nl}}^1(\omega)|$ holds for $n > 1$. In this case, from (14), the reset-triggered signal $z_s(t)$ can be approximated as $z_s(t) \approx z_{\mathrm{nl}}^1(t) + z_{\mathrm{bl}}(t)$, implying that that it predominantly comprises the first-order harmonic. Therefore, ensuring $\beta_n(\omega) \to 0$ supports the low-pass filtering assumption [24], [25], which is essential for ensuring the accuracy of the SIDF analysis.

However, due to the inherent nonlinearity of reset control systems, it is not feasible to completely eliminate high-order harmonics (i.e., achieve $\beta_n(\omega) = 0$).

Although high-order harmonics do not always cause issues, they can lead to multiple-reset actions in sinusoidal-input

closed-loop systems, compromising the accuracy of SIDF analysis and reducing the reliability of system design and performance predictions. In addition, dominated high-order harmonics increase the system's sensitivity to high-frequency disturbances and noise. To address this, we identify the multiple-reset frequency ranges as key areas where high-order harmonics should be reduced. Decreasing $\beta_n(\omega)$ in these ranges improves the accuracy of SIDF analysis and decreases the system's sensitivity to high-frequency noise.

According to (14) and (16), when the base-linear component $z_{\text{bl}}(t)$ remains constant, maintaining $\beta_n(\omega)$ within a bound less than 1, i.e., $\beta_n(\omega) \leq \sigma_\beta \in (0,1)$, ensures that the ratio $|Z^n_{\text{nl}}(\omega)|/|Z^1_{\text{nl}}(\omega)|$ remains within a controlled range, thereby limiting the impact of high-order harmonics.

Based on (16), to guide the design of a shaping filter $\mathcal{C}_s$ that achieves $\beta_n(\omega) = \sigma_\beta$, the magnitude condition for $\mathcal{C}_s$ is given as follows:

$$|\mathcal{C}_s(\omega)| = n\sigma_\beta / \left|\mathcal{T}_\beta(\omega) \cdot \mathbf{1}_{n_c \times 1}\right|. \tag{17}$$

Since the reset action is independent of the magnitude of $\mathcal{C}_s(\omega)$ [16], the value of n does not affect the system performance. By default, $n = 3$ is used in (17). Then, the following steps outline the design procedure for shaping filters in reset systems.

1) *Step 1:* Start by designing the reset control system with $\mathcal{C}_s(\omega) = 1$, and use Theorem 1 to identify the frequency range where multiple-reset actions occur.
2) *Step 2:* Then, select a value $\sigma_\beta \in (0,1)$, and design the shaping filter $|\mathcal{C}_s(\omega)|$ using (17) to achieve $\beta_n(\omega) = \sigma_\beta$ within the identified multiple-reset frequency range.
3) *Step 3:* Since the introduction of $\mathcal{C}_s(\omega)$ affects both the magnitude and phase of the first-order harmonics, adjusting other system parameters to compensate for these changes is needed in order to preserve the benefits of the first-order harmonic.

A detailed design procedure of an illustrative example following these steps is presented in Section VI.

VI. Illustrative Example: Designing a PID Shaping Filter to Reduce High-Order Harmonics in a CI-Based Reset Control System

This section presents the analysis and design procedure for a PID shaping filter to reduce high-order harmonics in a CI-based reset control system. The procedure is outlined as an illustrative case study.

The PCID control system, Case_1, with design parameters outlined in Section III, is chosen as the example due to its high-order harmonic issues, as shown in Fig. 7(a_1).

Following the steps outlined in Section V, Theorem 1 is applied to identify the multiple-reset frequency range for the PCID control system, Case_1, as $(0, 30)$ Hz. The value of 30 Hz is determined by sweeping the entire frequency range with a 1-Hz step size. For improved accuracy, smaller step resolutions can be utilized. Within this identified frequency range, reducing high-order harmonics is needed.

Next, by setting $\sigma_\beta = 0.6$ and applying equation (17), the resulting magnitude plot of $|\mathcal{C}_s(\omega)|$ is shown in Fig. 9. The value $\sigma_\beta = 0.6$ is chosen based on experimental evaluations to achieve improved system performance, as demonstrated in Section VII. In practice, other values of $\sigma_\beta \in (0,1)$ may also be selected, depending on the specific requirements for high-order harmonic reduction in the system.

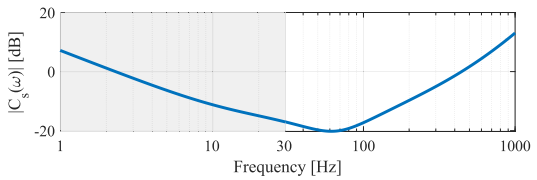

Fig. 9. Plot of $|\mathcal{C}_s(\omega)|$ meeting the condition of $\beta_n(\omega) = 0.6$ based on (17).

From Fig. 9, the shaping filter can be simplified as the LTI PI shaping filter, given by

$$\mathcal{C}_s(s) = 1 + \omega_\alpha / s \tag{18}$$

where $\omega_\alpha = 2\pi \cdot 30 = 60\pi$ [rad/s].

The objective of the shaping filter design is to attenuate high-order harmonics while preserving the benefits of the first-order harmonic. However, as shown in (6), the integration of the PI shaping filter impacts the phase of the HOSIDF of the reset controller. It is crucial to ensure that the shaping filter does not induce phase lag but instead introduces phase lead. The PID shaping filter $\mathcal{C}_s(s)$ reduces $\beta_n(\omega)$ in (16) for frequencies $\omega < \omega_\alpha$, while simultaneously introducing a phase lead at the bandwidth frequency of ω_{BW}, compared with the system without the shaping filter (i.e., $\mathcal{C}_s = 1$), by the following design:

$$\mathcal{C}_s(s) = k_s \cdot \left(1 + \frac{\omega_\alpha}{s}\right) \cdot \frac{s/\omega_\beta + 1}{s/\omega_\eta + 1} \cdot \frac{1}{s/\omega_\psi + 1} \tag{19}$$

with $\angle\mathcal{C}_s(\omega_{\text{BW}})$ meets the conditions [26]

$$\angle\mathcal{C}_s(\omega_{\text{BW}}) \in \left(k\pi, \frac{\pi}{2} - \arctan\left(\frac{\omega_c}{\omega_\alpha}\right) + k\pi\right), \quad k = -1, 0. \tag{20}$$

Since reset actions are amplitude-independent [16], the value of $k_s \neq 0 \in \mathbb{R}$ does not impact system performance. By default, $k_s = 1$. The introduction of the derivative element in (19) may amplify high-frequency noise, potentially causing multiple-reset actions. Therefore, the low-pass filter is incorporated to attenuate high-frequency components in $z_s(t)$. The cutoff frequency ω_ψ for the LPF is chosen based on the characteristics of the noise present in practice. In this study, reset systems incorporating the shaping filter from (19) are termed PID-shaped reset control systems.

CI-based reset systems, including Case_1, are built upon the generalized CI. Therefore, the phase margin introduced by the PID shaping filter in the CI-based reset system is first applied to the shaped CI and then propagated throughout the entire system. Remark 3 illustrates the phase lead imparted by the PID shaping filter to the shaped CI.

Remark 3: From (6), the phase lead introduced by the shaping filter in (19) to a shaped CI is given by

$$\phi_{\text{lead}} = \phi_s(\omega_{\text{BW}}) - \phi_0 \tag{21}$$

where $\phi_s(\omega_{\text{BW}})$ denotes the phase margin of the shaped CI system when the shaping filter $\mathcal{C}_s(s)$ in (19) is applied, and ϕ_0

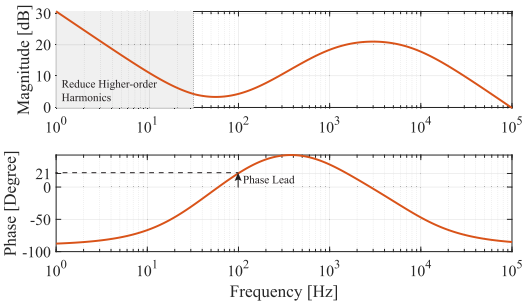

Fig. 10. Bode plot of the shaping filter $\mathcal{C}_s(s)$.

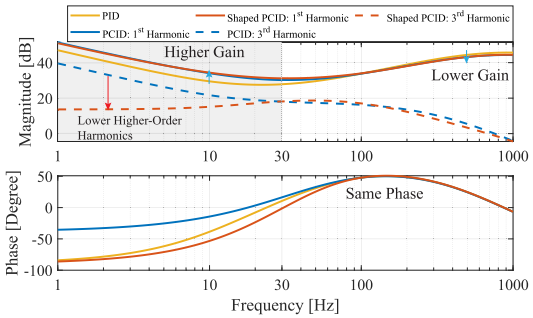

Fig. 11. Bode plots of the PID controller, the first-order and third-order harmonics in the PCID, and shaped PCID controllers. The multiple-reset region $(0, 30)$ Hz identified for the PCID system using Theorem 1 is shaded in gray.

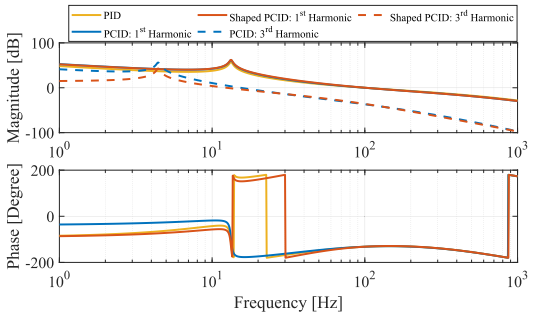

Fig. 12. Bode plots of the open-loop PID control system and the first- and third-order harmonics in the open-loop PCID and shaped PCID control systems on the precision motion stage $\mathcal{P}(s)$.

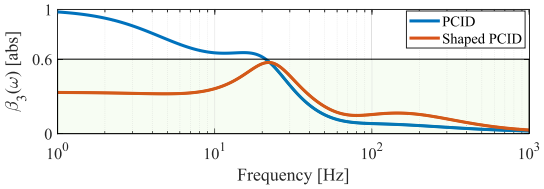

Fig. 13. plot of $\beta_3(\omega)$ in the closed-loop PCID and shaped PCID control systems.

refers to the phase margin of the generalized CI when $\mathcal{C}_s(s) = 1$. These phase margins are given by (22), as shown at the bottom of the page.

Based on (19), the shaping filter $\mathcal{C}_s(s)$ for Case$_1$ is designed with the following parameters: $\omega_\alpha = 60\pi$ [rad/s], $\omega_\beta = 1.05 \cdot \omega_{\text{BW}} = 659.7$ rad/s, $\omega_\eta = 12 \cdot \omega_{\text{BW}} = 7.5 \times 10^3$ rad/s, $\omega_\psi = 75 \cdot \omega_{\text{BW}} = 4.7 \times 10^4$ rad/s, and $k_s = 213$. The Bode plot of $\mathcal{C}_s(s)$ is shown in Fig. 10. At frequencies $\omega < \omega_\alpha$, $\mathcal{C}_s(s)$ functions as a PI controller. Note that due to the integral property of the shaping filter, the reset-triggered signal $z_s(t)$ may exhibit an offset and lack zero-crossings in the presence of an integral buffer. In such cases, the system behaves linearly. However, this linearization does not degrade performance; rather, it enhances performance, as linear control outperforms reset control in the low-frequency range in this case study. In addition, the integrator can be tamed to prevent buffer buildup at high frequencies as shown in Fig. 10.

In addition, the phase of the shaping filter at the bandwidth frequency $\omega_{\text{BW}} = 200\pi$ [rad/s] is $\angle\mathcal{C}_s(\omega_{\text{BW}}) = 21°$. Without the shaping filter, the CI with $\gamma = 0$ has a phase of $\phi_0 = -38.1°$ at $\omega_{\text{BW}} = 200\pi$ [rad/s], as determined using (22). In contrast, by applying the designed shaping filter $\mathcal{C}_s(s)$, the phase of the shaped CI improves to $\phi_s = -27.4°$, introducing a phase lead of $\phi_{\text{lead}} = 10.7°$ in the PCID control system, as calculated from (21). To preserve the phase margin and gain properties of the first-order harmonic, the parameters are set to $\omega_r = 141.4$ rad/s, $\gamma = 0.13$, and $k_r = 1.02$. Under these settings, the phase lead is $\phi_{\text{lead}} = 0°$.

Applying the designed PID shaping filter, the Bode plots for the PID, PCID, and shaped PCID controllers—showing both first- and third-order harmonics—are provided in Fig. 11. Then, Fig. 12 provides the corresponding Bode plots when these controllers are applied to the plant $\mathcal{P}(s)$ in (7). Collectively, these figures demonstrate that the shaped PCID control system reduces high-order harmonics within the frequency range of (0, 30) Hz, while preserving the gain and phase benefits of the first-order harmonic, compared with the PCID control system. It is worth noting that the PID shaping filter amplifies high-order harmonics in certain frequency ranges—such as [30, 100] Hz in this case study, as shown in Fig. 11. However, this amplification remains minimal, and within this range, the first-order harmonics are also enhanced. As a result, system performance is not degraded, which will be verified by the experimental results presented in Section VII.

Moreover, the plots of $\beta_3(\omega)$ for both the closed-loop PCID and shaped PCID control systems are shown in Fig. 13. The shaped PCID control system reduces $\beta_3(\omega)$, ensuring that $\beta_3(\omega) < 0.6$. Note that in this shaped PCID control system, the values of $\beta_n(\omega)$ for $n > 3$ are smaller than $\beta_3(\omega)$ and,

$$\begin{aligned}\phi_0 &= \arctan\left(-\pi\left(1+\gamma\right)/\left(4\left(1-\gamma\right)\right)\right)\\ \phi_s\left(\omega_{\text{BW}}\right) &= \arctan\left(\frac{4\left(1-\gamma\right)\sin\left(\angle\mathcal{C}_s\left(\omega_{BW}\right)\right)\cos\left(\angle\mathcal{C}_s\left(\omega_{BW}\right)\right)-\pi\left(1+\gamma\right)}{4\left(1-\gamma\right)\cos^2\left(\angle\mathcal{C}_s\left(\omega_{BW}\right)\right)}\right).\end{aligned} \tag{22}$$

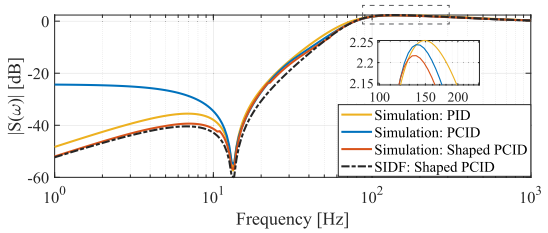

Fig. 14. Plots of simulated $\|e\|_\infty/\|r\|_\infty$ for the PID, PCID, and shaped PCID control systems, alongside the SIDF-predicted $\|e\|_\infty/\|r\|_\infty$ for the shaped PCID control system.

TABLE II

$\|e\|_\infty/\|r\|_\infty$ VALUES FOR THE PCID AND SHAPED PCID SYSTEMS UNDER SINUSOIDAL INPUTS AT FREQUENCIES OF 5, 10, 30, AND 200 HZ

Systems	Input Frequencies [Hz]			
	5	10	30	200
PID	1.5×10^{-2}	1.3×10^{-2}	1.7×10^{-1}	1.28
PCID	4.8×10^{-2}	1.9×10^{-2}	1.6×10^{-1}	1.26
Shaped PCID	1.0×10^{-2}	8.9×10^{-3}	1.5×10^{-1}	1.25
Precision Improvement	79.17%	53.16%	6.25%	0.79%

for clarity, are not displayed. However, they can be computed using (16).

The results shown in Figs. 11–13 indicate that the PID shaping filter designed in this study reduces high-order harmonics while maintaining the advantages of the first-order harmonic in the PCID system. These improvements are anticipated to enhance the accuracy of SIDF analysis and improve the steady-state precision of the PCID system. Further validation of these enhancements will be provided through simulations and experimental results in Section VII.

VII. EVALUATION OF THE EFFECTIVENESS OF THE SHAPED RESET CONTROL SYSTEM VIA SIMULATIONS AND EXPERIMENTS

This section presents simulation and experimental results to validate the effectiveness of the PID-shaped reset system designed in Section VI in comparison to both linear and reset systems, as applied to the precision motion stage in Fig. 2.

A. Simulation Results: Enhanced Steady-State Performance and Improved Accuracy of Sidf Analysis

To evaluate the closed-loop performance of the shaped PCID control system, Fig. 14 presents the simulated $\|e\|_\infty/\|r\|_\infty$ (8) for the PID, PCID, and shaped PCID systems. The shaped PCID system demonstrates the lowest $\|e\|_\infty/\|r\|_\infty$ compared with the other two systems, indicating improved precision. This enhancement is attributed to the shaped PCID control system's superior gain properties in the first-order harmonic compared with the PID control system, while reducing high-order harmonics relative to the PCID control system, as demonstrated in Figs. 11 and 12.

Table II presents a quantitative comparison of $\|e\|_\infty/\|r\|_\infty$ for the PID, PCID, and shaped PCID systems at selected frequencies: 5, 10, 30, and 200 Hz. The choice of 5, 10, and 30 Hz validates the improved precision resulting from high-order harmonics reduction in the shaped PCID system within the targeted frequency range of $(0, 30)$ Hz. In addition, the inclusion of 200 Hz ensures that high-frequency precision has also been attained. Across all frequencies, the shaped PCID system consistently exhibits lower steady-state errors, highlighting its effectiveness.

TABLE III

RPE OF THE SIDF ANALYSIS FOR PCID AND SHAPED PCID CONTROL SYSTEMS AT FREQUENCIES OF 1, 10, 50, 100, 500, AND 1000 HZ

Systems	Input Frequencies [Hz]					
	1	10	50	100	500	1000
PCID	15.51	0.97	0.03	0.02	2.35×10^{-3}	3.21×10^{-3}
Shaped PCID	0.03	0.18	0.02	0.01	8.39×10^{-4}	3.15×10^{-3}

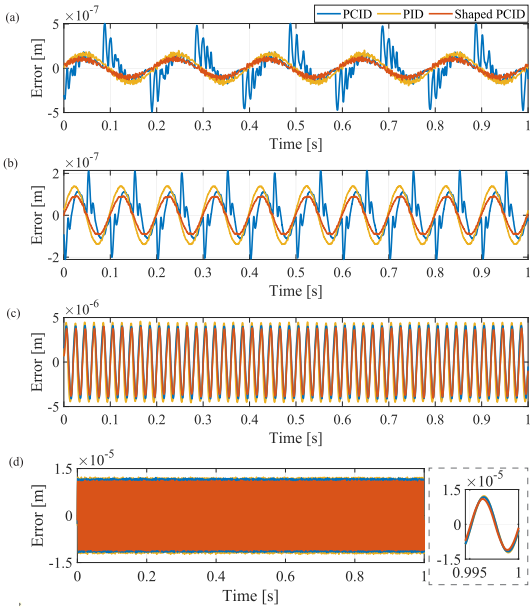

Fig. 15. Normalized experimental measured steady-state errors of the PID, PCID, and shaped PCID control systems under sinusoidal inputs $r(t) = 1 \times 10^{-5}\sin(2\pi t)$ [m], shown for (a) $f = 5$ Hz, (b) $f = 10$ Hz, (c) $f = 30$ Hz, and (d) $f = 100$ Hz.

Another observation from Fig. 14 is that the SIDF analysis provides more reliable predictions for the shaped PCID system compared with the PCID system in Fig. 6. Define the relative prediction error (RPE) of the SIDF analysis as RPE $= \||\mathcal{S}_{\text{sim}}(\omega)| - |\mathcal{S}_{\text{sidf}}(\omega)|\|/|\mathcal{S}_{\text{sidf}}(\omega)|$, where $|\mathcal{S}_{\text{sim}}(\omega)|$ and $|\mathcal{S}_{\text{sidf}}(\omega)|$ are obtained from simulations and SIDF analysis (8), respectively. A comparison of RPE values across six frequencies, shown in Table III, supports this observation. The improved reliability of the SIDF analysis in the shaped PCID system is attributed to the high-order harmonics reduction. However, discrepancies between SIDF predictions and simulations remain, as the SIDF considers only the first-order harmonic. To address this, $\beta_n(\omega) \to 0$ can be restricted to maintain the two-reset condition, and HOSIDF methods in [14] and [15], can be employed for higher accuracy.

B. Experimental Results: Improved Steady-State Tracking Precision

Fig. 15 illustrates the experimentally measured steady-state errors for the PID, PCID, and shaped PCID systems

TABLE IV

MAXIMUM STEADY-STATE ERRORS $\|e\|_\infty$ [M] IN THE PCID SYSTEM AND SHAPED PCID SYSTEMS UNDER SINGLE SINUSOIDAL INPUTS AT FREQUENCIES OF 5, 10, 30, AND 200 HZ

Systems	Input Frequency [Hz]			
	5	10	30	200
PID	2.03×10^{-7}	1.41×10^{-7}	1.72×10^{-6}	1.23×10^{-5}
PCID	5.03×10^{-7}	2.16×10^{-7}	1.65×10^{-6}	1.21×10^{-5}
Shaped PCID	1.38×10^{-7}	9.30×10^{-8}	1.56×10^{-6}	1.14×10^{-5}
Precision Improvement	72.56%	56.94%	5.45%	7.00%

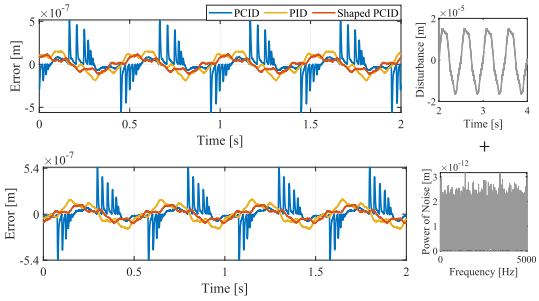

Fig. 16. Experimental measured steady-state errors of PID, PCID, and shaped PCID control systems under $d_1(t) + n(t)$.

in response to a normalized sinusoidal input signal defined as $r(t) = 1 \times 10^{-5} \sin(2\pi f t)$ [m], with frequencies $f = 5$, 10, 30, and 200 Hz. Note that during practical experiments, the magnitudes of input signals employed for these four frequencies were different; however, for the purposes of comparison, the magnitude of all input signals has been normalized to 1×10^{-5} [m].

Table IV presents the maximum steady-state errors at the three test frequencies for the PID, PCID, and shaped PCID systems. The results demonstrate that the shaped PCID system achieves the lowest position errors among the three systems, especially at the low frequency range of (0, 30) Hz. Notably, at 5 Hz, the shaped PCID system improves precision by 72.56% compared with the PCID system.

Real-world input signals are often more complex than a single sinusoid. In this section, the results of the single sinusoidal reference inputs serve to illustrate the steady-state performance of the three systems across varying frequencies. To comprehensively evaluate the positioning performance of the shaped reset control system, multiple inputs—including disturbances and noise—will be applied to the three systems in Section VII-C.

C. Experimental Results: Improved Steady-State Tracking Precision and Disturbance and Noise Rejection

This section presents the steady-state errors of three systems under multiple input conditions.

Fig. 16(a) shows the measured steady-state errors of the three systems in response to a disturbance input signal defined as $d_1(t) = 1 \times 10^{-7}[149.3 \sin(4\pi t) + 1.2 \sin(16\pi t) + 11.9 \sin(16\pi t) + 3.0 \sin(40\pi t)]$ [m].

Next, a white noise input $n(t)$ with a power bound of 3×10^{-12} [m] is added to the disturbance input $d_1(t)$. The resulting steady-state errors for the three systems are presented in Fig. 16(b). Table V summarizes the maximum steady-state errors for the PID, PCID, and shaped PCID systems under these inputs. The results show that the shaped PCID system improves precision by 80.07% compared with the PCID system, effectively rejecting both the disturbance and noise.

TABLE V

MAXIMUM STEADY-STATE ERRORS $\|e\|_\infty$ [M] IN THE PID, PCID, AND SHAPED PCID CONTROL SYSTEMS UNDER DIFFERENT INPUT SIGNALS

Systems	Input Signals		
	$d_1(t) + n(t)$	$r_2(t) + d_2(t) + n(t)$	$r_3(t) + d_3(t) + n(t)$
PID	1.80×10^{-7}	1.22×10^{-7}	1.17×10^{-7}
PCID	5.52×10^{-7}	3.63×10^{-7}	2.00×10^{-7}
Shaped PCID	1.10×10^{-7}	8.80×10^{-8}	9.64×10^{-8}
Precision Improvement	80.07%	75.78%	51.79%

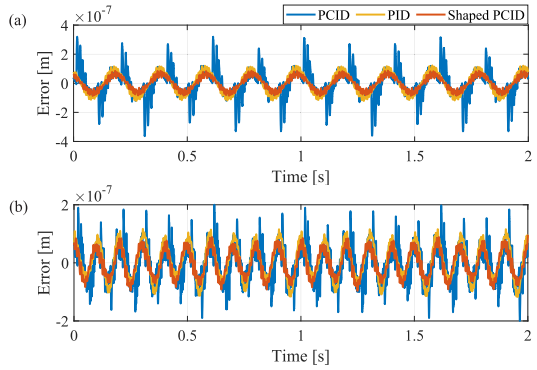

Fig. 17. Experimental measured steady-state errors of PID, PCID, and shaped PCID control systems under (a) $r_2(t) + d_2(t) + n(t)$ and (b) $r_3(t) + d_3(t) + n(t)$.

To evaluate both the reference tracking, as well as the disturbance and noise rejection of the closed-loop shaped PCID control system, Fig. 17 compares the steady-state errors of the PID, PCID, and shaped PCID systems under multiple input signals. In Fig. 17(a), the inputs include a reference signal $r_2(t) = 6 \times 10^{-6} \sin(10\pi t)$ [m], alongside the disturbance $d_2(t) = 1 \times 10^{-8}[49.0 \sin(4\pi t) + 5.5 \sin(16\pi t) + 1.1 \sin(40\pi t)]$ [m] and white noise $n(t)$ with a power bound of 3×10^{-12} [m]. In Fig. 17(b), the inputs consist of a reference signal $r_3(t) = 6 \times 10^{-6} \sin(20\pi t)$ [m], a disturbance $d_3(t) = 1 \times 10^{-7}[2.7 \sin(10\pi t) + 3.7 \sin(14\pi t) + 3.0 \sin(30\pi t)]$ [m], and the white noise noise $n(t)$ with a power bound of 3×10^{-12} [m]. The maximum steady-state errors for these two cases are summarized in Table V, indicating that the shaped PCID system improves precision by 73.5% and 53.06% in the two scenarios, respectively.

Moreover, Fig. 18 illustrates the control inputs for these two cases, demonstrating that the shaped PCID system requires the least control input force while achieving the lowest steady-state error. Together, Figs. 17 and 18 highlight the improved control efficiency of the shaped PCID system, which can be attributed to the reduction of high-order harmonics.

D. Experimental Results: Eliminated Limit Cycle

The PID shaping filter can also effectively eliminate limit cycles observed in the step responses of reset PID systems. A detailed proof is provided in Appendix D. Current solutions for

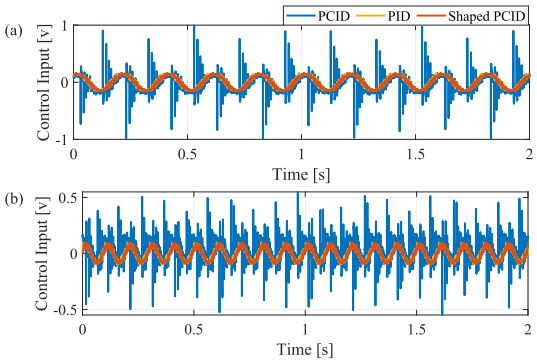

Fig. 18. Experimental measured control input of PID, PCID, and shaped PCID control systems under (a) $r_2(t) + d_2(t) + n(t)$ and (b) $r_3(t) + d_3(t) + n(t)$.

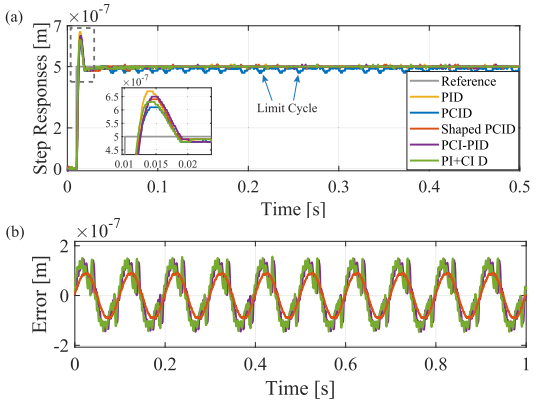

Fig. 19. Experimental measured. (a) Step responses of PID, PCID, shaped PCID, PCI-PID, PI+CI D control systems. (b) Steady-state errors of the PCI-PID, PI+CI D, and shaped PCID control systems under sinusoidal input $r(t) = 1 \times 10^{-5} \sin(20\pi t)$ [m].

addressing the limit cycle problem include the PI+CI structure [27] and the PCI-PID structure in Fig. 4. To provide a fair comparison of the effectiveness of five control structures—PID, PCID, shaped PCID, PI+CI D, and PCI-PID—we designed these systems with the same bandwidth of 100 Hz and phase margin of 50° of the first-order harmonics for fair comparison.

Fig. 19(a) presents the step responses of the five systems, highlighting the effectiveness of the shaped PCID, PI+CI D, and PCI-PID systems in mitigating the limit cycle issues observed in the PCID system. These systems also exhibit lower overshoot compared with the PID system. However, the PI+CI D and PCI-PID structures address limit cycle problems at the cost of reduced steady-state performance.

For example, as shown in Fig. 19(b), under a sinusoidal input signal $r(t) = 1 \times 10^{-5} \sin(20\pi t)$ [m], the steady-state errors of the PI+CI D and PCI-PID systems are larger than those of the shaped PCID system. This occurs because the PI+CI D and PCI-PID systems exhibit dominated high-order harmonics at low frequencies, similar to the PCID system. In contrast, the shaped PCID system reduces these high-order harmonics, leading to improved steady-state performance.

In summary, the proposed shaped PCID control system improves positioning accuracy and control efficiency compared with both PID and PCID control systems on the precision motion stage. In addition, it effectively eliminates limit cycles, leading to enhanced overall system performance.

VIII. Conclusion

In conclusion, this article makes two main contributions. First, it introduces a method for identifying multiple-reset and two-reset regions in sinusoidal-input closed-loop reset systems, providing engineers with a practical tool to evaluate the reliability of SIDF analysis. The effectiveness and time-saving advantages of this method have been validated through simulations and experimental results across two case studies.

Second, the study introduces a shaped reset control strategy to reduce high-order harmonics. As an illustrative example, the procedure for designing a PID shaping filter in CI-based reset systems is presented. The resulting PID-shaped reset control system reduces high-order harmonics while preserving the benefits of the first-order harmonic compared with the reset control system. Experimental results from precision motion stages highlight three key benefits of the PID-shaped reset system: 1) improved SIDF analysis accuracy; 2) enhanced tracking precision, disturbance and noise rejection, and overall control efficiency; and 3) elimination of limit-cycle issues in the step responses of reset systems.

Future research could explore the application of the shaped reset control system design in Section V to other reset control structures, aiming to investigate further improvements in system performance.

Appendix A
Proof of Lemma 1

Proof: Consider a closed-loop reset control system in Fig. 1 under a sinusoidal reference input $r(t) = |R|\sin(\omega t)$, and satisfying Assumption 2.

Within each steady-state period $(0, 2\pi/\omega]$, the reset instant t_i is defined as the time at which the reset-triggered signal $z_s(t_i)$ reaches zero. Let $x_i(t)$, $m_i(t)$, $z_i(t)$, and $z_s^i(t)$ represent the state of the reset controller $\mathcal{C}_r$, the reset output, the reset input, and the reset-triggered signal, during the intervals $(t_{i-1}, t_i]$, where $i \in \mathbb{Z}^+$, respectively. This proof presents the piecewise expressions for the steady-state trajectories of the system, following the three steps outlined below.

Step 1 [Derive the Piecewise Expression for $x_i(t)$]:

From (1), the system operates without any reset actions during the time interval $(t_{i-1}, t_i]$. At the reset instant $t_i \in J$, the state $x_i(t_i)$ undergoes a reset (or jump) to a new state $x_i(t_i^+)$, given by

$$x_i\left(t_i^+\right) = A_\rho x_i\left(t_i\right). \tag{23}$$

The jump in (23) introduces a step input signal $h_i(t)$ into the system, impacting the trajectories during the subsequent time interval $(t_i, t_{i+1}]$ [15]. The signal $h_i(t)$ is given by

$$h_i\left(t\right) = \left[x_i\left(t_i^+\right) - x_i\left(t_i\right)\right] h\left(t - t_i\right) = \left(A_\rho - I\right) x_i\left(t_i\right) h\left(t - t_i\right) \tag{24}$$

where $h(t)$ is a unit step signal given by

$$h\left(t\right) = \begin{cases} 1, & t > 0 \\ 0, & t \le 0 \end{cases} \tag{25}$$

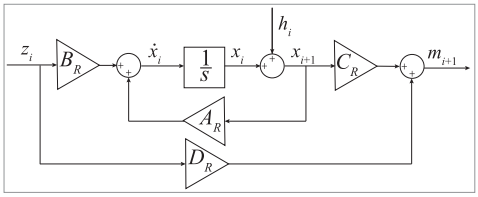

Fig. 20. State-space block diagram of $\mathcal{C}_r$ during the time interval $(t_i,\ t_{i+1}]$.

with the Fourier transform $H(\omega) = \mathscr{F}[h(t)] = (j\omega)^{-1}$.

Based on (1) and (24), the block diagram of the controller $\mathcal{C}$ for the time interval $(t_i, t_{i+1}]$ is illustrated in Fig. 20, where the signal $x_{i+1}(t)$ is derived from two inputs: $z_i(t)$ and $h_i(t)$. The respective contributions to $x_{i+1}(t)$ from $z_i(t)$ and $h_i(t)$ are labeled as $x^z_{i+1}(t)$ and $x^h_{i+1}(t)$, respectively.

Under Assumption 2, the system's steady-state trajectories are guaranteed to have well-defined Fourier transforms. Let $Z_i(\omega)$, $H_i(\omega)$, $X_i(\omega)$, $X^z_{i+1}(\omega)$, and $X^h_{i+1}(\omega)$ represent the Fourier transforms of the signals $z_i(t)$, $h_i(t)$, $x_i(t)$, $x^z_{i+1}(t)$, and $x^h_{i+1}(t)$, respectively.

Since no reset actions occur during the time interval $(t_i, t_{i+1}]$, the superposition law holds. Therefore, $X_{i+1}(\omega)$ is express as

$$\begin{aligned} &X_{i+1}(\omega) \\ &= X^z_{i+1}(\omega) + X^h_{i+1}(\omega) \\ &= X^z_{i+1}(\omega) Z_i(\omega)^{-1} \cdot Z_i(\omega) + X^h_{i+1}(\omega) H_i(\omega)^{-1} \cdot H_i(\omega). \end{aligned} \tag{26}$$

Based on Figs. 1 and 20, within the closed-loop reset system, when $h_i(t) = 0$, we have

$$X^z_{i+1}(\omega) Z_i(\omega)^{-1} = (j\omega I - A_R)^{-1} B_R \tag{27}$$

and when $z_i(t) = 0$, it follows that:

$$X^h_{i+1}(\omega) H_i(\omega)^{-1} = \mathcal{S}_{\mathrm{bl}}(\omega)(j\omega I - A_R)^{-1} j\omega. \tag{28}$$

By combining (26), (27), and (28), we derive

$$\begin{aligned} X_{i+1}(\omega) = (j\omega I - A_R)^{-1} B_R Z_i(\omega) + \mathcal{S}_{\mathrm{bl}}(\omega) \\ \cdot (j\omega I - A_R)^{-1} j\omega H_i(\omega). \end{aligned} \tag{29}$$

According to (1), during the reset interval $(t_i, t_{i+1}]$, we obtain $X_i(\omega) = (j\omega I - A_R)^{-1} B_R Z_i(\omega)$. Substituting this $X_i(\omega)$ into (29) yields

$$X_{i+1}(\omega) = X_i(\omega) + \mathcal{S}_{\mathrm{bl}}(\omega)(j\omega I - A_R)^{-1} j\omega H_i(\omega). \tag{30}$$

From (24), the Fourier transform of $h_i(t)$ is given by

$$H_i(\omega) = \mathscr{F}[h_i(t)] = \left(A_\rho - I\right)(j\omega)^{-1} e^{-j\omega t_i} x_i(t_i). \tag{31}$$

Substituting (31) into (30), we obtain

$$X_{i+1}(\omega) = X_i(\omega) + \mathcal{T}_s(\omega) e^{-j\omega t_i} x_i(t_i) \tag{32}$$

where

$$\mathcal{T}_s(\omega) = \mathcal{S}_{\mathrm{bl}}(\omega)(j\omega I - A_R)^{-1}\left(A_\rho - I\right). \tag{33}$$

Conducting the Fourier transforms of equation (32), we obtain

$$\begin{aligned} &x_{i+1}(t) \\ &= x_i(t) + h_s(t - t_i)\, x_i(t_i), \text{where } h_s(t) = \mathscr{F}^{-1}[\mathcal{T}_s(\omega)]. \end{aligned} \tag{34}$$

Till here, the state of the reset controller during the time interval $(t_i, t_{i+1}]$ denoted as $x_{i+1}(t)$ is derived.

Step 2 [Derive the Piecewise Expression for $z_i(t)$]:

Similar to Step 1, from Fig. 20, the signal $m_{i+1}(t)$ is derived from two inputs: $z_i(t)$ and $h_i(t)$. The contributions to the output $m_{i+1}(t)$ from $z_i(t)$ and $h_i(t)$ are denoted as $m^z_{i+1}(t)$ and $m^h_{i+1}(t)$, respectively. Let $M_i(\omega)$, $M^z_{i+1}(\omega)$, and $M^h_{i+1}(\omega)$ represent the Fourier transforms of the signals $m_i(t)$, $m^z_{i+1}(t)$, and $m^h_{i+1}(t)$, respectively. Using the same calculation process as in Step 1, $M_{i+1}(\omega)$ is expressed as

$$M_{i+1}(\omega) = M^z_{i+1}(\omega) Z_i(\omega)^{-1} \cdot Z_i(\omega) + M^h_{i+1}(\omega) H_i(\omega)^{-1} \cdot H_i(\omega) \tag{35}$$

where

$$\begin{aligned} M^z_{i+1}(\omega) Z_i(\omega)^{-1} &= C_R(j\omega I - A_R)^{-1} B_R + D_R = \mathcal{C}_l(\omega) \\ M^h_{i+1}(\omega) H_i(\omega)^{-1} &= \mathcal{S}_{\mathrm{bl}}(\omega) C_R(j\omega I - A_R)^{-1} j\omega. \end{aligned} \tag{36}$$

Substituting (36) into (35), $M_{i+1}(\omega)$ is simplified to

$$M_{i+1}(\omega) = \mathcal{C}_l(\omega) Z_i(\omega) + \mathcal{S}_{bl}(\omega) C_R (j\omega I - A_R)^{-1} j\omega H_i(\omega). \tag{37}$$

From (1), during the reset interval $(t_i, t_{i+1}]$, we have

$$M_i(\omega) = \mathcal{C}_l(\omega) Z_i(\omega). \tag{38}$$

Substituting (31) and (38) into (37), $M_{i+1}(\omega)$ is given by

$$M_{i+1}(\omega) = M_i(\omega) + C_R \mathcal{T}_s(\omega) e^{-j\omega t_i} x_i(t_i). \tag{39}$$

From Fig. 1, in the closed-loop reset system, the following relation holds:

$$\begin{aligned} Z_i(\omega) &= R(\omega) - (A(\omega) + M_i(\omega))\mathcal{C}_\sigma(\omega) \\ Z_{i+1}(\omega) &= R(\omega) - \left(A(\omega) + M_{i+1}(\omega)\right)\mathcal{C}_\sigma(\omega) \end{aligned} \tag{40}$$

where $A(\omega) = \mathscr{F}[a(t)]$ and

$$\mathcal{C}_\sigma(\omega) = \mathcal{C}_3(\omega)\mathcal{P}(\omega)\mathcal{C}_4(\omega)\mathcal{C}_1(\omega). \tag{41}$$

From (40), the following equations are derived:

$$\begin{aligned} M_i(\omega) &= [R(\omega) - Z_i(\omega)] \cdot \mathcal{C}_\sigma(\omega)^{-1} - A(\omega) \\ M_{i+1}(\omega) &= \left[R(\omega) - Z_{i+1}(\omega)\right] \cdot \mathcal{C}_\sigma(\omega)^{-1} - A(\omega). \end{aligned} \tag{42}$$

Substituting $M_{i+1}(\omega)$ and $M_i(\omega)$ from (42) into (39), $Z_{i+1}(\omega)$ is obtained as

$$Z_{i+1}(\omega) = Z_i(\omega) - \mathcal{T}_\alpha(\omega) e^{-j\omega t_i} x_i(t_i) \tag{43}$$

where

$$\mathcal{T}_\alpha(\omega) = \mathcal{C}_\sigma(\omega) C_R \mathcal{T}_s(\omega). \tag{44}$$

Conducting the Fourier transforms of equation (43), we obtain

$$\begin{aligned} &z_{i+1}(t) \\ &= z_i(t) - h_\alpha(t - t_i)\, x_i(t_i), \text{where } h_\alpha(t) = \mathscr{F}^{-1}[\mathcal{T}_\alpha(\omega)]. \end{aligned} \tag{45}$$

Till here, the input of the reset controller during the time interval $(t_i, t_{i+1}]$ denoted as $z_{i+1}(t)$ is derived.

Step 3 [Derive the Piecewise Expression for $z^i_s(t)$]:

During the reset intervals $(t_{i-1}, t_i]$ and $(t_i, t_{i+1}]$, no reset action takes place. Let $Z^i_s(\omega)$ denotes the Fourier transforms of $z^i_s(t)$. Therefore, the following relationship holds:

$$Z^i_s(\omega) = \mathcal{C}_s(\omega) Z_i(\omega), \text{and } Z^{i+1}_s(\omega) = \mathcal{C}_s(\omega) Z_{i+1}(\omega). \tag{46}$$

Substituting (46) into (43), we obtain

$$Z_s^{i+1}(\omega) = Z_s^i(\omega) - \mathcal{C}_s(\omega)\,\mathcal{T}_\alpha(\omega)\,e^{-j\omega t_i}x_i(t_i). \tag{47}$$

Conducting the Fourier transforms of equation (47), we obtain

$$z_s^{i+1}(t) = z_s^i(t) - h_\beta(t-t_i)\,x_i(t_i) \tag{48}$$

where

$$h_\beta(t) = \mathscr{F}^{-1}\left[\mathcal{C}_s(\omega)\,\mathcal{T}_\alpha(\omega)\right]. \tag{49}$$

Till here, the expression of the reset-triggered signal during the time interval $(t_i, t_{i+1}]$ denoted as $z_s^{i+1}(t)$ is derived. We conclude the proof. □

APPENDIX B
PROOF OF THEOREM 1

Proof: Consider the reset control system shown in Fig. 1 with a sinusoidal reference input $r(t) = |R|\sin(\omega t)$ and satisfies Assumptions 2 and 3. This proof derives the multiple-reset conditions in the sinusoidal-input reset system. It is organized into three steps as follows.

Step 1 (Derive the First Reset Instant t_1 Within One Steady-State Cycle):

Under Assumption 3, the state and reset-triggered signal of the reset system during the interval $(0, t_1]$, denoted as $x_1(t)$ and $z_s^1(t)$, are equivalent to those of its BLS, denoted as $x_{\rm bl}(t)$ and $z_{\rm bl}(t)$, respectively, as expressed by

$$\begin{aligned} x_1(t) &= x_{\rm bl}(t) = |R\Theta_{\rm bl}(\omega)|\sin\left(\omega t + \angle\Theta_{\rm bl}(\omega)\right) \\ z_s^1(t) &= z_{\rm bl}(t) = |R\mathcal{S}_{\rm ls}(\omega)|\sin\left(\omega t + \angle\mathcal{S}_{\rm ls}(\omega)\right) \end{aligned} \tag{50}$$

where $\angle\Theta_{\rm bl}(\omega) \in (-\pi,\ \pi]$ and $\angle\mathcal{S}_{\rm ls}(\omega) \in (-\pi,\ \pi]$. Functions $\Theta_{\rm bl}(\omega)$ and $\mathcal{S}_{\rm ls}(\omega)$ are given in (11).

From Assumption 3 and (50), the first reset instant denoted as t_1 within one steady-state cycle, which corresponds to the first zero-crossing point of the reset-triggered signal $z_s^1(t)$, is expressed as

$$t_1 = \begin{cases} (\pi - \angle\mathcal{S}_{\rm ls}(\omega))/\omega, & \text{if } \angle\mathcal{S}_{\rm ls}(\omega) \in (0,\ \pi] \\ (-\angle\mathcal{S}_{\rm ls}(\omega))/\omega, & \text{if } \angle\mathcal{S}_{\rm ls}(\omega) \in (-\pi,\ 0]. \end{cases} \tag{51}$$

From (51), we have $t_1 \le \pi/\omega$.

Step 2 [Establish the Condition for Multiple-Reset Systems: The Reset Triggered Signal $z_s^2(t)$ Must Exhibit at Least One Zero-Crossing Within the Interval $(t_1, \pi/\omega)$]:

Under Assumption 2, within a steady-state period $(0, 2\pi/\omega]$, we obtain two conclusions.

1) At the time instant t_1 and $t_1 + \pi/\omega$, we have $z_s(t_1) = z_s(t_1 + \pi/\omega) = 0$.
2) Since t_1 represents the first reset instant within a steady-state cycle $(0, 2\pi/\omega]$, there is no zero-crossings of $z_s(t)$ in the both the time intervals $(0, t_1)$ and $(\pi/\omega, t_1 + \pi/\omega)$.

From these two conclusions, Fig. 21 shows the green area that has no reset actions within a steady-state period $(0, 2\pi/\omega]$.

A system is classified as a multiple-reset system if it exhibits more than two zero-crossings per $2\pi/\omega$ steady-state cycle in response to a sinusoidal reference input $r(t) = |R|\sin(\omega t)$. If the reset-triggered signal $z_s(t)$ has no zero-crossings within the interval $(t_1, \pi/\omega)$, it will lack zero-crossings within

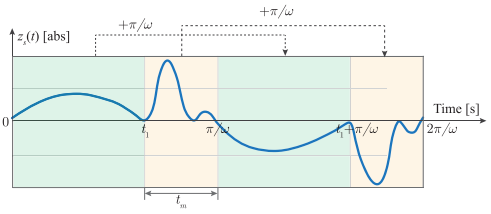

Fig. 21. Plot of the steady-state reset-triggered signal $z_s(t)$, with regions of the same color indicating the same number of zero-crossings and opposite-sign trajectories. Green areas indicate no zero-crossings, while yellow areas show regions with zero-crossings.

$(t_1 + \pi/\omega, 2\pi/\omega)$. This results in exactly two zero-crossings at t_1 and $t_1 + \pi/\omega$ over one steady-state cycle, $(0, 2\pi/\omega]$.

Therefore, a system exhibits multiple-reset behavior if the reset-triggered signal $e_s(t)$ has at least one zero-crossing within $(t_1, \pi/\omega)$, as illustrated in the yellow-shaded area of Fig. 21.

From Lemma 1, $z_s(t)$ can be broken down into piecewise components $z_s^i(t)$ over intervals $(t_i, t_{i+1}]$. Thus, for $z_s(t)$ to have at least one zero-crossing within $(t_1, \pi/\omega)$, the second piece $z_s^2(t)$ must include at least one zero-crossing within the interval $t \in (t_1, \pi/\omega)$.

Step 3 (Formulate the Multiple-Reset Condition):

From (10), the reset-triggered signal $z_s^2(t)$ during the time interval $(t_1, t_2]$ can be expressed as

$$z_s^2(t) = z_s^1(t) - h_\beta(t-t_1)\,x_1(t_1), \text{for } t \in (t_1, t_2]. \tag{52}$$

From (50) and (51), $x_1(t_1)$ is given by

$$\begin{aligned} x_1(t_1) &= |R\Theta_{\rm bl}(\omega)|\sin\left(\omega t_1 + \angle\Theta_{\rm bl}(\omega)\right) \\ &= \begin{cases} |R|\cdot\Theta_s(\omega), & \text{if } \angle\mathcal{S}_{\rm ls}(\omega) \in (0,\ \pi] \\ -|R|\cdot\Theta_s(\omega), & \text{if } \angle\mathcal{S}_{\rm ls}(\omega) \in (-\pi,\ 0] \end{cases} \end{aligned} \tag{53}$$

where

$$\Theta_s(\omega) = |\Theta_{\rm bl}(\omega)|\sin\left(\angle\mathcal{S}_{\rm ls}(\omega) - \angle\Theta_{\rm bl}(\omega)\right). \tag{54}$$

By defining $t = t_\delta + t_1$ and substituting $x_1(t_1)$ from (53) into (52), along with $z_s^1(t)$ defined from (50), we obtain

$$z_s^2(t_\delta + t_1) = \begin{cases} -|R|\Delta(t_\delta), & \text{if } \angle\mathcal{S}_{\rm ls}(\omega) \in (0,\ \pi] \\ |R|\Delta(t_\delta), & \text{if } \angle\mathcal{S}_{\rm ls}(\omega) \in (-\pi,\ 0] \end{cases} \tag{55}$$

where

$$\Delta(t_\delta) = |\mathcal{S}_{\rm ls}(\omega)|\sin(\omega t_\delta) + h_\beta(t_\delta)\,\Theta_s(\omega). \tag{56}$$

The multiple-reset condition requires that $z_s^2(t)$ has at least one zero-crossing within the time interval $(t_1, \pi/\omega)$. Using the relation $t = t_\delta + t_1$ and from (55), this condition is transformed to: there exists a time interval $t_\delta \in (0, \pi/\omega - t_1)$ such that $z_s^2(t_\delta + t_1)$ has at least one zero-crossing.

From (51), the value of $\pi/\omega - t_1$ is given by

$$\pi/\omega - t_1 = \begin{cases} (\angle\mathcal{S}_{\rm ls}(\omega))/\omega, & \text{if } \angle\mathcal{S}_{\rm ls}(\omega) \in (0,\ \pi] \\ (\pi + \angle\mathcal{S}_{\rm ls}(\omega))/\omega, & \text{if } \angle\mathcal{S}_{\rm ls}(\omega) \in (-\pi,\ 0]. \end{cases} \tag{57}$$

From (57), $\pi/\omega - t_1$ can be expressed as

$$t_m = \pi/\omega - t_1 = \angle\mathcal{S}_{\rm ls}(\omega)/\omega + \pi/\omega \cdot \text{sign}\left(\mathcal{S}_{\rm ls}(\omega)\right) \tag{58}$$

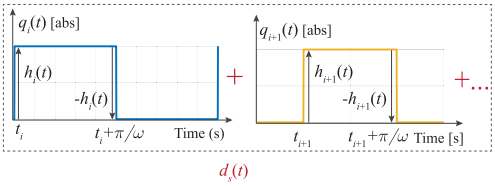

Fig. 22. Plots of signals $q_i(t)$ in (62) and $d_s(t)$ in (66).

where

$$\operatorname{sign}(x)=\begin{cases}0, & \text{if } x>0\\ 1, & \text{if } x\le 0.\end{cases} \tag{59}$$

Since a zero-crossing is independent of amplitude, the multiple-reset condition is simplified to verifying the existence of a time interval $t_\delta \in (0,t_m)$ such that $\Delta(t_\delta)=0$. This completes the proof. □

Appendix C
Proof of Lemma 2

Proof: Consider a closed-loop reset control system as shown in Fig. 1, with a sinusoidal reference input $r(t)=|R|\sin(\omega t)$ and satisfying Assumptions 2 and 3. This proof demonstrates that the steady-state reset-triggered signal $z_s(t)$ is composed of a base-linear component $z_{\mathrm{bl}}(t)$ and a nonlinear component $z_{\mathrm{nl}}(t)$, where $z_{\mathrm{nl}}(t)$ is obtained by filtering a stair-step signal $d_s(t)$ through an LTI transfer function. The proof is organized into three steps.

Step 1 (Prove that Reset Actions Introduce Square Waves into Systems):

The state $x_c(t)$ of the reset controller $\mathcal{C}_r$ is nonlinear and can be represented as the sum of its harmonics [28], expressed as

$$x_c(t)=\sum_{n=1}^{\infty}x_{\mathrm{cn}}(t)=|X_{\mathrm{cn}}|\sin(n\omega t+\angle X_{\mathrm{cn}}) \tag{60}$$

where $|X_{\mathrm{cn}}|$ and $\angle X_{\mathrm{cn}}$ represent the magnitude and phase of each harmonic $x_{\mathrm{cn}}(t)$ in $x_c(t)$.

From (60), the following relation holds:

$$x_c(t_i)=-x_c(t_i\pm\pi/\omega). \tag{61}$$

At each reset instant t_i, according to (24), the state $x_c(t_i)$ undergoes a jump to $A_\rho x_c(t_i)$, generating a step input defined by $h_i(t)=(A_\rho-I)x_c(t_i)\,h(t-t_i)$.

Then, based on (61), a step input with an opposite sign $h_i'(t)=-h_i(t)=-(A_\rho-I)x_c(t_i)\,h(t-t_i\pm\pi/\omega)$ is introduced at the time instant $t_i+\pi/\omega$. Signals $h_i(t)$ and $-h_i(t)$ together produce a square wave signal over each steady-state cycle, beginning at t_i with an amplitude of $(A_\rho-I)x_i(t_i)$ and a period of $2\pi/\omega$, as illustrated in Fig. 22.

Step 2 (Formulate the Square Waves):

The square wave introduced at the time instants t_i and $t_i+\pi/\omega$ is expressed as

$$q_i(t)=\left(A_\rho-I\right)x_c(t_i)\,q(t-t_i) \tag{62}$$

where $q(t)$ is a square wave with an amplitude of 1 and a period of $2\pi/\omega$, defined as

$$q(t)=\sum_{n=1}^{\infty}2\cdot\sin(n\omega t)/n\pi,\quad n=2k+1,k\in\mathbb{N}. \tag{63}$$

From (62) and (63), $q_i(t)$ is expressed as

$$q_i(t)=\sum_{n=1}^{\infty}q_i^n(t) \tag{64}$$

where

$$q_i^n(t)=2\left(A_\rho-I\right)x_c(t_i)\sin(n\omega(t-t_i))/(n\pi). \tag{65}$$

Step 3 [Illustrate that Square Waves $q_i(t)$ Combine to Form a Stair-Step Signal $d_s(t)$, Contributing to the Reset-Triggered Signal $z_s(t)$]:

At each reset instant t_i within the half-cycle $(0,\pi/\omega]$, a square wave $q_i(t)$ is introduced. Let the number of reset instants within each half-cycle $(0,\pi/\omega]$ be denoted by μ. From (64) and (65), a stair-step signal $d_s(t)$ is generated within one $2\pi/\omega$ period. This signal is illustrated in Fig. 22 and is expressed as

$$d_s(t)=\sum_{i=1}^{i=\mu}q_i(t)=\sum_{i=1}^{i=\mu}\sum_{n=1}^{\infty}q_i^n(t). \tag{66}$$

From (66), $d_s(t)$ can be written as

$$d_s(t)=\sum_{n=1}^{\infty}\sum_{i=1}^{i=\mu}q_i^n(t). \tag{67}$$

Define $d_s^n(t)$ as the nth harmonic of $d_s(t)$, from (65) and (67), $d_s(t)$ is expressed as

$$\begin{aligned}d_s(t)&=\sum_{n=1}^{\infty}d_s^n(t)\\ d_s^n(t)&=2\left(A_\rho-I\right)/(n\pi)\cdot\sum_{i=1}^{i=\mu}x_c(t_i)\sin(n\omega(t-t_i))\end{aligned} \tag{68}$$

with their Fourier transforms given by

$$\begin{aligned}D_s(\omega)&=\sum_{n=1}^{\infty}D_s^n(\omega)\\ D_s^n(\omega)&=2\left(A_\rho-I\right)/(n\pi)\cdot\sum_{i=1}^{i=\mu}\mathscr{F}\left[x_c(t_i)\sin(n\omega(t-t_i))\right].\end{aligned} \tag{69}$$

Under Assumption 3, the reset-triggered signal $z_s(t)$ initially follows its base-linear trajectory $z_{\mathrm{bl}}(t)$ within the interval $(0,t_1)$, as defined in (14). At time t_1, reset actions introduce a stair-step signal $d_s(t)$ into the system. By replacing the signal $h_i(t)$ (whose Fourier transform is $H_i(\omega)=1/(j\omega)$) with the stair-step signal $d_s(t)$ (whose Fourier transform is $D_s(\omega)$) in Fig. 20, and following the derivation process outlined in Appendix A, the nonlinear component $z_{\mathrm{nl}}(t)$ is derived. Finally, $z_{\mathrm{bl}}(t)$ and $z_{\mathrm{nl}}(t)$ combine to form $z_s(t)$, as expressed in (14). This concludes the proof. □

Appendix D
Proof of Theorem 2

Proof: Consider a closed-loop reset control system as illustrated in Fig. 1, with a sinusoidal reference input $r(t)=|R|\sin(\omega t)$, satisfying Assumptions 2 and 3. This proof derives the magnitude ratio of the higher order harmonics (for $n>1$)

relative to the first-order harmonic (for $n = 1$) in the nonlinear component $z_{\rm nl}(t)$ as defined in (14).

From (14) and (15), the signal $z^n_{\rm nl}(t)$, representing the nth harmonic component of $z_{\rm nl}(t)$, is given by

$$z^n_{\rm nl}(t) = -\mathscr{F}^{-1}\left[\mathcal{C}_s(n\omega)\,\mathcal{T}_\beta(n\omega)\,D^n_s(\omega)\right]. \tag{70}$$

From (70), the Fourier transform of $z^n_{\rm nl}(t)$ is given by

$$Z^n_{\rm nl}(\omega) = -\mathcal{C}_s(n\omega)\,\mathcal{T}_\beta(n\omega)\,D^n_s(\omega). \tag{71}$$

From (69) and (71), we obtain

$$\beta_n(\omega) = \frac{\left|Z^n_{\rm nl}(\omega)\right|}{\left|Z^1_{\rm nl}(\omega)\right|} = \frac{\left|\mathcal{C}_s(n\omega)\,\mathcal{T}_\beta(n\omega)\right|}{n\left|\mathcal{C}_s(\omega)\,\mathcal{T}_\beta(\omega)\right|}. \tag{72}$$

Here, the proof is concluded. □

Appendix E
Proof of Limit Cycle Elimination Using the PID Shaping Filter

Proof: This proof demonstrates that the PID shaping filter effectively eliminates limit cycle issues in the step responses of reset control systems.

Consider a closed-loop reset control system in Fig. 1 subjected to an unit step input $h(t)$, with the Laplace transform of $h(t)$ given by $H(s) = 1/s$. In this system, the final value of $z_s(t)$ denoted by $\lim_{t\to\infty} z_s(t)$ is given by

$$\begin{aligned}\mathcal{S}_\alpha(s) &= \mathcal{C}_1(s)\,\mathcal{S}_{\rm bl}(s)\\ \lim_{t\to\infty} z_s(t) &= \lim_{s\to 0} s\cdot Z_s(s) = \lim_{s\to 0} s\,\mathcal{C}_s(s)\,\mathcal{C}_1(s)\,\mathcal{S}_{\rm bl}(s)\cdot 1/s\\ &= \lim_{s\to 0}\mathcal{C}_s(s)\,\mathcal{S}_\alpha(s).\end{aligned} \tag{73}$$

In the reset systems with the shaping filter $\mathcal{C}_s(s) = 1$, limit cycles occur when the reset-triggered signal continues to trigger the reset actions at steady states, characterized by

$$\lim_{t\to\infty} z_s(t) = \lim_{s\to 0}\mathcal{S}_\alpha(s) = 0 \tag{74}$$

while the reset controller's output $m(t)$ does not settle to a steady-state equilibrium at zero; instead, it continues to oscillate persistently around certain nonzero values as $t \to \infty$, i.e.,

$$\lim_{t\to\infty} m(t) = \lim_{s\to 0} s\mathcal{C}_1(s)\,\mathcal{C}_l(s)\,\mathcal{S}_{\rm bl}(s)\,1/s = \text{constant} \neq 0. \tag{75}$$

The following content demonstrates that the PID shaping filter, as defined in (19), can eliminate limit cycle issues in reset systems.

The PID shaping filter $\mathcal{C}_s(s)$ in (19) can be expressed as

$$\begin{aligned}\mathcal{C}_s(s) &= F(s)/s\\ F(s) &= k_s\cdot(s+\omega_\alpha)\cdot\frac{s/\omega_\beta+1}{s/\omega_\eta+1}\cdot\frac{1}{s/\omega_\psi+1}.\end{aligned} \tag{76}$$

With the PID shaping filter in (76), $\lim_{t\to\infty} z_s(t)$ in (73) is written as

$$\lim_{t\to\infty} z_s(t) = \lim_{s\to 0} F(s)\cdot\mathcal{S}_\alpha(s)/s. \tag{77}$$

From (76), the value of $F(s)$ as $s \to 0$ is given by

$$\lim_{s\to 0} F(s) = k_s\cdot\omega_\alpha = \text{constant} \neq 0. \tag{78}$$

From (74), the transfer function $\mathcal{S}_\alpha(s)$ can be expressed in terms of polynomial terms, given by

$$\begin{aligned}\mathcal{S}_\alpha(s) &= \frac{n_1 s^n + n_2 s^{n-1} + \cdots + n_q s}{m_1 s^m + m_2 s^{m-1} + \cdots + m_q}\\ &\quad n_1,\ldots,n_q,m_1,\ldots,m_q \in \mathbb{R},\quad m_q \neq 0,\ n_q \neq 0.\end{aligned} \tag{79}$$

From (79), we find that

$$\begin{aligned}\lim_{s\to 0}\frac{\mathcal{S}_\alpha(s)}{s} &= \lim_{s\to 0}\frac{n_1 s^{n-1} + n_2 s^{n-2} + \cdots + n_q}{m_1 s^m + m_2 s^{m-1} + \cdots + m_q}\\ &= n_q/m_q = \text{constant} \neq 0.\end{aligned} \tag{80}$$

Combining (77), (78), and (80), we derive

$$\lim_{t\to\infty} z_s(t) = \lim_{s\to 0} F(s)\cdot\mathcal{S}_\alpha(s)/s = \text{constant} \neq 0. \tag{81}$$

Thus, from (81), by applying the PID shaping filter $\mathcal{C}_s(s)$, as specified in (19), the limit-cycle behaviors in reset systems are eliminated. □

References

[1] R. M. Schmidt, G. Schitter, and A. Rankers, *The Design of High Performance Mechatronics: High-Tech Functionality by Multidisciplinary System Integration*. Amsterdam, The Netherlands: IOS Press, 2020.

[2] L. Chen, N. Saikumar, S. Baldi, and S. H. HosseinNia, "Beyond the waterbed effect: Development of fractional order CRONE control with non-linear reset," in *Proc. Annu. Amer. Control Conf. (ACC)*, Jun. 2018, pp. 545–552.

[3] B. Wilamowski and J. D. Irwin, *Control and Mechatronics*. Boca Raton, FL, USA: CRC Press, 2018.

[4] J. C. Clegg, "A nonlinear integrator for servomechanisms," *Trans. Amer. Inst. Electr. Eng., II, Appl. Ind.*, vol. 77, no. 1, pp. 41–42, Mar. 1958.

[5] Y. Guo, Y. Wang, and L. Xie, "Frequency-domain properties of reset systems with application in hard-disk-drive systems," *IEEE Trans. Control Syst. Technol.*, vol. 17, no. 6, pp. 1446–1453, Nov. 2009.

[6] Y. Guo, Y. Wang, L. Xie, H. Li, and W. Gui, "Optimal reset law design of reset control systems with application to HDD systems," in *Proc. 48h IEEE Conf. Decis. Control (CDC), 28th Chin. Control Conf.*, Dec. 2009, pp. 5287–5292.

[7] F. S. Panni, H. Waschl, D. Alberer, and L. Zaccarian, "Position regulation of an EGR valve using reset control with adaptive feedforward," *IEEE Trans. Control Syst. Technol.*, vol. 22, no. 6, pp. 2424–2431, Nov. 2014.

[8] R. Beerens, A. Bisoffi, L. Zaccarian, W. P. M. H. Heemels, H. Nijmeijer, and N. van de Wouw, "Reset integral control for improved settling of PID-based motion systems with friction," *Automatica*, vol. 107, pp. 483–492, Sep. 2019.

[9] G. Zhao, D. Nešić, Y. Tan, and C. Hua, "Overcoming overshoot performance limitations of linear systems with reset control," *Automatica*, vol. 101, pp. 27–35, Mar. 2019.

[10] N. Saikumar, R. K. Sinha, and S. H. HosseinNia, "'Constant in gain lead in phase' element—Application in precision motion control," *IEEE/ASME Trans. Mechatronics*, vol. 24, no. 3, pp. 1176–1185, Jun. 2019.

[11] A. Barreiro, A. Baños, and E. Delgado, "Reset control of the double integrator with finite settling time and finite jerk," *Automatica*, vol. 127, May 2021, Art. no. 109536.

[12] N. Karbasizadeh and S. H. HosseinNia, "Continuous reset element: Transient and steady-state analysis for precision motion systems," *Control Eng. Pract.*, vol. 126, Sep. 2022, Art. no. 105232.

[13] P. W. J. M. Nuij, O. H. Bosgra, and M. Steinbuch, "Higher-order sinusoidal input describing functions for the analysis of non-linear systems with harmonic responses," *Mech. Syst. Signal Process.*, vol. 20, no. 8, pp. 1883–1904, Nov. 2006.

[14] N. Saikumar, K. Heinen, and S. H. HosseinNia, "Loop-shaping for reset control systems: A higher-order sinusoidal-input describing functions approach," *Control Eng. Pract.*, vol. 111, Aug. 2021, Art. no. 104808.

[15] X. Zhang, M. B. Kaczmarek, and S. H. HosseinNia, "Frequency response analysis for reset control systems: Application to predict precision of motion systems," *Control Eng. Pract.*, vol. 152, Nov. 2024, Art. no. 106063.
[16] A. Banos and A. Barreiro, *Reset Control Systems*. Cham, Switzerland: Springer, 2012.
[17] E. A. Barabanov and A. V. Konyukh, "Bohl exponents of linear differential systems," *Mem. Differ. Equ. Math. Phys.*, vol. 24, pp. 151–158, May 2001.
[18] O. Beker, C. V. Hollot, Y. Chait, and H. Han, "Fundamental properties of reset control systems," *Automatica*, vol. 40, no. 6, pp. 905–915, Jun. 2004.
[19] Y. Guo et al., *Analysis and Design of Reset Control Systems*, vol. 11. Edison, NJ, USA: IET, 2015.
[20] A. A. Dastjerdi, A. Astolfi, N. Saikumar, N. Karbasizadeh, D. Valério, and S. H. HosseinNia, "Closed-loop frequency analysis of reset control systems," *IEEE Trans. Autom. Control*, vol. 68, no. 2, pp. 1146–1153, Feb. 2023.
[21] S. A. Hosseini and S. H. HosseinNia, "Frequency domain stability and convergence analysis for general reset control systems architecture," 2025, *arXiv:2502.09309*.
[22] N. Karbasizadeh, A. A. Dastjerdi, N. Saikumar, and S. H. HosseinNia, "Band-passing nonlinearity in reset elements," *IEEE Trans. Control Syst. Technol.*, vol. 31, no. 1, pp. 333–343, Jan. 2023.
[23] N. Karbasizadeh and S. H. HosseinNia, "Stacking integrators without sacrificing the overshoot in reset control systems," in *Proc. Amer. Control Conf. (ACC)*, Jun. 2022, pp. 893–899.
[24] W. E. V. Velde et al., *Multiple-input Describing Functions and Nonlinear System Design*. New York, NY, USA: McGraw-Hill, 1968.
[25] H. K. Khalil and J. W. Grizzle, *Nonlinear Systems, Volume 3*. Upper Saddle River, NJ, USA: Prentice-Hall, 2002.
[26] X. Zhang and S. H. HosseinNia, "Enhancing reset control phase with lead shaping filters: Applications to precision motion systems," 2025, *arXiv:2503.15020*.
[27] A. Baños and A. Vidal, "Definition and tuning of a PI+CI reset controller," in *Proc. Eur. Control Conf. (ECC)*, Jul. 2007, pp. 4792–4798.
[28] A. Pavlov, N. Van De Wouw, and H. Nijmeijer, *Uniform Output Regulation of Nonlinear Systems: A Convergent Dynamics Approach, Volume 205*. Cham, Switzerland: Springer, 2006.

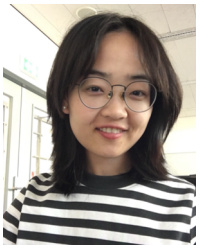

Xinxin Zhang (Member, IEEE) received the M.S. degree in precision instruments engineering from Tianjin University, Tianjin, China, in 2020, and the Ph.D. degree in precision and microsystems engineering from Delft University of Technology, Delft, The Netherlands, in 2025.

She is currently a Post-Doctoral Researcher with the Department of Applied Physics and Electronics, Umea University, Umea, Sweden. Her research interests include frequency response analysis of reset feedback control systems, the design of reset controllers for precision motion systems, and robot control.

S. Hassan HosseinNia (Senior Member, IEEE) received the Ph.D. degree (cum laude) in electrical engineering in 2013, specializing in automatic control and its applications in mechatronics.

He is currently a faculty member at Delft University of Technology (TU Delft), where he leads advanced research in precision mechatronic system design, high-performance motion control, active vibration damping, and the design and control of electromagnetic and piezoelectric actuators. His contributions have been recognized internationally. Through his work, he brings a forward-looking perspective that bridges theoretical depth with industrial applicability, fostering innovation in advanced control and mechatronic system design. His current research focuses on developing innovative control strategies and system architectures to enhance bandwidth and precision in next-generation mechatronic systems. He has published extensively in leading journals and conferences.

Dr. Hosseinnia served as the General Chair of the 7th IEEE International Conference on Control, Mechatronics, and Automation (ICCMA 2019). He also serves on the editorial boards of *IFAC Mechatronics, Control Engineering Practice* and *Fractional Calculus and Applied Analysis*. In 2024, he received the Abel Young Scientists Award from the 12th IFAC Conference on Fractional Differentiation and its Applications.